ARL-TR-23 AR-008-409

DEPARTMENT OF DEFENCE

DEFENCE SCIENCE AND TECHNOLOGY ORGANISATION

AERONAUTICAL RESEARCH LABORATORY

MELBOURNE, VICTORIA

Technical Report 23

ASSESSMENT OF IMPACT DAMAGE IN COMPOSITE STRUCTURES

by

R. JONES
S.C. GALEA
J.J. PAUL

Approved for public release.

DECEMBER 1993

AR-008-409

DEPARTMENT OF DEFENCE
DEFENCE SCIENCE AND TECHNOLOGY ORGANISATION
AERONAUTICAL RESEARCH LABORATORY

Technical Report 23

ASSESSMENT OF IMPACT DAMAGE IN COMPOSITE STRUCTURES

by

R. JONES
S.C. GALEA
J.J. PAUL

SUMMARY

In order to provide through-life support for structural components fabricated from advanced composite materials, it is desirable to establish a damage tolerance methodology. There are many difficulties in meeting this objective, including the multiplicity of failure modes, the numerous types of potentially significant defects which may arise during manufacture or in service, and the sensitivity to moisture and temperature. This paper focuses on the problem of impact damage and reviews research undertaken at ARL in recent years related to the analysis and testing of impact damage composite laminates. It is shown that the residual strength of impact damaged laminates reduces to an asymptotic limit as the size of the damage increases and that uniaxial S-N curves for damaged laminates have a generic shape with a pronounced threshold (endurance) level.

Recent developments in the bonded repair of impact damage are also discussed and a simple repair methodology is presented. This methodology is then illustrated via a laboratory test program and by a repair to a damaged F/A-18 Horizontal Stabilator.

DSTO AUSTRALIA

POSTAL ADDRESS: **Director, Aeronautical Research Laboratory**
506 Lorimer Street, Fishermens Bend
Victoria 3207, Australia.

TABLE OF CONTENTS

Page Nos.

1. INTRODUCTION

Graphite-epoxy composites have many advantages for use as aircraft structural materials, including their formability, high specific strength and stiffness, resistance to cracking by fatigue loading and their immunity to corrosion. Thus, besides producing lighter, more efficient structures, the use of composites should provide more durable structures compared with those manufactured from conventional aluminium alloys. Graphite-epoxy composites, while having the above advantages, are prone to a fairly wide range of defects and damage which may significantly reduce residual strength [1-6]. Of the various types of defects, delaminations (i.e. single or multiple internal cracks whose planes are parallel to the surface of a component) [7-9] arising in service are probably the most insidious because they can cause reductions in compressive strength (up to 65% of undamaged strength [10,11]) and are difficult to detect. Delaminations may develop during service due to the presence of excessive inter-laminar shear stresses or through-the-thickness tensile stresses at holes, free edges, in the region of section changes, and in bonded joints. However, perhaps the most important source of delaminations is impact. Such damage can occur from dropped tools or from stones thrown up from the runway. While impact can cause a significant amount of delamination, often the only external indication is a very slight surface indentation [12,13]. This type of damage is frequently referred to as 'barely visible impact damage' (BVID). The problem of BVID is of particular concern because the damage is unlikely to be discovered unless the region is subjected to non-destructive inspection (NDI), such as ultrasonic C-scanning. However, unfortunately, most routine NDI is likely to be confined to potential hot spots such as critical joints. Frequent full-scale NDI is costly and time-consuming.

It is highly desirable that procedures are available so that the possible occurrence of delamination-type defects is allowed for in the design and certification of composite aircraft structures and in the development of approaches for through-life support, to provide a rationale for setting inspection intervals, particularly for highly stressed regions and also provide repair/reject criteria [14,15].

This paper discusses the analysis and testing of impact damaged graphite/epoxy laminates, and their ability to provide information to establish a rationale for inspection intervals.

2. CHARACTERISATION OF DELAMINATION RESISTANCE

A detailed review of the damage tolerance of impact damaged composites was given in [1]. The conclusions of this and other subsequent studies are summarised below.

Damage Nature

- Compressive residual strength (RS) following impact damage reduced to less than 40% (-3000 to -4000 με) of the undamaged strength
- BVID can have a similar RS to visible damage
- BVID RS is lower than that for a drilled hole of the same size
- Artificial flaws have higher RS than BVID

Damage Size/Extent

- BVID produces an initial large drop in the RS then a gradual reduction to an asymptotic limit
- Artificial disbonds also have an initial large drop to a constant RS
- Bonded step lap joints behave in the same generic fashion as monolithic laminates

Damage Location

- Work is required on representative geometries including joints
- Work is required on multiple impact locations

Laminate, Matrix State

- Moisturised laminates have increased impact resistance
- The effect of moisture (hot/wet) is to lower RS by approximately 15 percent

Laminate Stacking Sequence

- Artificial flaws are more damaging if the outer plies are 0°
- Dispersed plies may improve RS

Component Size and Geometry

- Large components do not always experience similar RS to laboratory specimens

Stress-Field

- Majority of the work reported uses uniaxial loading
- Consideration must be given to representative bi-axial loads

Environment

- Relative RS increases under hot/wet conditions
- Freeze/thaw cycling may not always increase damage

Prior Service History

- RS may initially increase and then decrease under cycling
- Peak compressive cyclic stress are the main influence
- More information is required on representative loading and truncation of load spectra

Damage Growth

- Artificial flaws, when near surface, exhibit marked growth
- Artificial flaws deep in laminate may not grow
- Impact damage usually grows only slightly

It should be noted that, as shown in [1], experimental tests and analytical studies have shown that for delaminations in (a) composite laminates [33,34,35], (b) at step lap joints [76,77], or (c) at mechanically fastened composite joints, a stage is reached after which a significant increase in the size of the damage does not significantly reduce the residual strength. This significantly simplified the methodology for estimating critical damage size and dramatically reduces the size of the required static strength test program.

Delamination in composites is generally a mixed mode fracture process with inter-laminar tensile and shear stresses at the delamination front. The inter-laminar tensile stresses give rise to a Mode I component (with the associated energy released rate G_I), and the inter-laminar shear stresses give rise to a Mode II component (with energy release rate G_{II}). When using the energy release rate approach to characterise delamination, it must be remembered that the growth will often be both mixed-mode and non-self-similar.

In attempting to formulate suitable failure criteria based on the energy release rate method, many researchers have designed a variety of experiments for laminated plates with the intention of isolating and characterising pure Mode I, pure Mode II, and mixed-mode failure. A selection of results are discussed in the next section.

2.1. Mode I Characterisation

There has been considerable success in characterising Mode I delaminations. The methods most popularly used are the Double Cantilever Beam (DCB) test and the free-Edge Delamination Tensile (EDT) test. The results of these tests on comparable material systems, by various researchers, are briefly summarised in Table 1a. It can be seen that the values of G_{Ic} are fairly consistent within the type of test method employed, varying between 80 and 240 J/m^2, depending on the matrix material and the nature of the fibre-matrix interface. In interpreting the values of G_{Ic} from DCB specimens, attention should be given to the surface morphology of the delamination area, since extensive fibre bridging [16] or intra-ply cracking [17] can influence the value of the energy release rate obtained so that it is higher than the value that would have been obtained if the delamination was entirely confined within the matrix-rich region and the plane of initial delamination.

Table 1b briefly describes some of the experimental and data analysis techniques used by researchers in estimating the value of G_{Ic}. For the DCB tests, three methods of analysis are commonly used: they are an analysis based on beam theory, [16, 18-21] the area under load displacement curve method [22] and a semi-empirical compliance method [17]. All three methods give reasonable results. The edge delamination tensile specimen has received quite a lot of attention, notably from O'Brien [23,24]. Laminated plate theory and the simple rule of mixtures to compute the stiffness loss due to delaminations have been used to obtain an expression relating the critical energy release rate G_c to the critical strain ε_c measured at the onset of delamination. The values of G_c so obtained are often only slightly higher than the value obtained through DCB specimens [22]. This is not surprising since, in EDT specimens, the delaminations initiate at the free-edge where high peel stresses are present, essentially resulting in predominantly Mode I fracture. A disadvantage of EDT-type tests is that they often produce intra-ply cracking as well as delamination, resulting in complex fracture surface morphologies rather than the 'clean' delamination surfaces encountered in unidirectional DCB tests. An attempt to modify the EDT specimen by introducing starter delaminations in the form of inserts has resulted in considerable lowering of the value of G_{Ic} [25]. Further, it has also been shown that G_{Ic} obtained through EDT specimens is sensitive to differences in specimen widths [25] (see Table 1a).

The 90° Centre Notch (CN) specimen has also been used by a number of researchers [22,26]. This method relies on the computation of the stress intensity factor K_{Ic} which is, in turn, related to G_{Ic} through an expression involving material constants. Although the experimental and analytical procedures of the 90° CN test are very different from those

of the EDT or DCB tests, the values of G_{Ic} obtained through these methods agree reasonable well, perhaps indicating that at least for Mode I behaviour, the test methodologies are acceptable.

2.2. Mode II Characterisation

The situation with Mode II delamination is unfortunately very different. There is wide variability of results for G_{IIc} in the literature for comparable composite systems. Table 2 shows that the variation of G_{IIc} obtained ranges from 154 to 1042 J/m^2. The experiments designed to measure G_{IIc} are often derived from tests to determine shear strength. Although the Cracked Lap Shear (CLS) specimen has been used to determine G_{IIc}, it is essentially a mixed-mode specimen. The proportion of G_{II} present in this test has been determined, through finite element analyses, to be between 75% and 80% of the total system energy release rate [18,19]. Since the Cracked Lap Shear specimen is a mixed-mode specimen, the value of G_{IIc} is dependent on the failure criterion used [19] and the accuracy of the finite element analysis in determining the proportions of G_I and G_{II}.

Some researchers have attempted to obtain G_{IIc} more directly through pure Mode II tests. Russell & Street [20,27] have used an edge delaminated laminate specimen simply loaded as a beam specimen. Chatterjee's [32] three-point bend test was similar except that two delaminations were introduced instead of one and were located in the flexural compressive region of the specimen. Chatterjee, however, reported values of G_{IIc} about twice the value of those obtained by Russell & Street. Jurf & Pipes [29] modified the Arcan test fixtures and used them to test a single edge notch specimen. Because of the nature of the geometry required, this specimen had to be about 90 plies thick and bonded to an aluminium fixture. The main advantage of the Arcan test was that it enabled Mode I, Mode II and Mixed-Mode testing on a single specimen type. However, there was also a tendency for some specimens to fail at the fixture-specimen adhesive bond, thus rendering the test invalid. Donaldson [26] investigated Mode II failure of a notched in-plane crack through a modified three-rail shear test arrangement. It may be argued that since both the growth of in-plane delaminations and along-the-fibre cracks in unidirectional laminates are matrix-dominated, the three-rail shear test should yield a G_{IIc} that is dependent only upon the matrix material.

2.3. Discussion of Test Results

Much work remains to be done to properly characterise delaminations in composite laminates, particularly their Mode II and Mixed-Mode behaviour. Various failure criteria proposed have met with only limited success in explaining mixed-mode failure. Much evidence suggests that G_{IIc} is much higher than G_{Ic}. In mixed-mode fracture, the contributions of Mode I and Mode II components to the total energy release rate are complicated and not readily apparent. In particular, the individual quantities of G_I and G_{II} cannot necessarily be simply added together to obtain the total energy release rate. This is because, in three-dimensional delamination propagation, the growth of the crack front is often non-self-similar, and furthermore the contribution of Mode II may become significant. The analyses and experiments carried out to date have concentrated mainly on the first two modes of failure, although for thicker non-unidirectional laminates, the contributions of Modes II and III became increasingly more significant than that of Mode I. Clearly a failure surface in three-dimensional (a failure envelope in two-dimensional) stress space needs to be developed. This goal is presently not yet attainable since there

does not appear to be a set of consistent data for mixed-mode fracture from different investigations. In proposing failure criteria, expressions often used are of the form:

$$\frac{G_I^m}{G_{Ic}^m} + \frac{G_{II}^n}{G_{IIc}^n} = 1 \qquad (1)$$

where m and n are constants. Although useful in curve-fitting the experimental data, such expressions lack feasible physical interpretations. Indeed the extension of such a law to three-dimensional failure, besides needing the value G_{IIIc}, has no physical backing. Any acceptable failure criteria based on energy release rates must have a sound physical basis and for the case of two-dimensional, self-similar growth, equation (1) must reduce to the form $G_{tot} = G_I + G_{II}$. This philosophy has the following implications:

(1) A consistent test methodology must be developed for both G_{IIc} and G_{IIIc}, and must allow for the effect of local constraint.

(2) Less emphasis should be given to the curve fitting approach for mixed-mode fracture.

(3) A detailed three-dimensional analysis should be undertaken for each test method in order to determine the relative contributions due to G_I, G_{II}, G_{III}.

3. FATIGUE LIFE PREDICTION

3.1. Test Results

Cyclic fatigue tests play a central role in the assessment of fatigue life and the specification of inspection intervals for metallic components. This has led to similar tests for composites with impact damage. It has been found that the *S-N* curves generated from experimental data are often flat over a large range of cycles [33-37]. Tension-tension fatigue loading is considered to be less critical than compression-compression and tension-compression loading [38 40]. This paper will concentrate on the latter two loading cases. For compression-compression and tension-compression loading, the maximum residual compressive load as a fraction of the static failure load (S) decreases from 1.0 to typically 0.6 for N in the range 1 to 10^6, depending on the initial damage size.

The greatest rate of degradation appears to be during the early part of cyclic loading, for N up to about 100 cycles. As the number of cycles, and hence the damage size is increased, very little further residual strength degradation is observed. In fact, it has been observed that S = 0·6 may be taken as the 'fatigue threshold' value, below which the component may be assumed to have 'infinite life.' Various researchers report threshold values of between 0.6 and 0.8 [11,32 35,41-44]. *S-N* curves are invariably drawn from a best fit of limited experimental data often with large scatter and their shapes vary from straight slopes to some form of curve.

The differences in fatigue lives resulting from changes in maximum compressive stress or strain from different researchers are summarised in Table 3. From the figures shown in the table, it can be seen that an uncertainty in the magnitude of the applied maximum compressive stress, for example 10%, can lead to a hundred-fold difference in fatigue life. Of particular interest is the considerable scatter in the data recorded by Ryder *et al.* [35] and Potter [34] which show an order of magnitude of difference in the fatigue lives of specimens at a nominally constant stress level.

For service aircraft the in-flight loads on a component will not be accurately known. There is often a significant variation between aircraft, with the result that the stress levels will always be subjected to a degree of uncertainty. We have seen that a small change in stress can result in a very large change in fatigue life. This implies that laboratory testing cannot be expected to provide accurate estimates of the fatigue lives of impact damage laminates and therefore cannot be expected to provide accurate information on inspection intervals. If this is true then the rationale for conducting such fatigue tests becomes questionable. Indeed, there are two natural consequences of this phenomenon:

(1) During the designing of a component, the stresses should be kept below the threshold (endurance) value, thus eliminating the possibility of a fatigue failure due to BVID.

(2) If an aircraft is already in service, and the design procedure had not included step (1), then the emphasis for research and development should be moved towards:

   (a) Static strength testing to determine critical damage size and loads, allowing for representative service conditions; and

   (b) developing a rational reject/repair criterion for the component which includes a methodology for determining inspection intervals.

Indeed, as a result of this work it is clear that further research is required in order to understand the physical reasons why the pronounced fatigue threshold (endurance limit) exists.

3.2. Prediction of Damage Growth

In order to characterise the delamination growth using fracture mechanics techniques, several recent investigations (see Chatterjee [47]; Mohlin *et al.* [48]; O'Brien [49]; Ramakumar & Whitcomb [50]; Wilkins *et al.* [18]) have adopted a growth law relationship of the type $(da/dN) = cG^n$ or $(da/dN) = c(\Delta G)^n$ where G is the mixed-mode delamination fracture energy, c and n are constants determined from experiments. Table 4 gives the value of the exponent n as predicted in several studies for different modes, that is Mode I, Mode II, and Mixed-Mode. At this point it is important to note that the values of the exponent n given in Table 4 are obtained by fitting a suitable curve to the experimental data. Hence, in order to get a good correlation for predicting the growth of a delamination, it is very important to obtain experimental data which are accurate and realistic. Table 4 reveals a large variation of n for Mode I loading and a relatively small variation for Mode II loading. Table 5 gives the values of n for Mode II which are taken from the experimental work by Russell & Street [52].

Indeed when evaluating the delamination fracture energy in different modes (that is G_I, G_{II}, and G_{III}) by analytical and experimental means there will be inherent errors which are somewhat beyond control. As shown in section 2 the measured values for G_{Ic} vary from 80 to 240 J/m^2 depending upon the matrix material and the nature of the fibre-matrix interface, and the variation of G_{Ic} in replicate measurements appear to be much greater than ±5%. For G_{II}, the situation is worse. The value of G_{IIc} depends very strongly on the test procedure and the data reduction scheme adopted (see section 2). Indeed Table 2 shows for T300/5208 a variation in G_{IIc} of between 154 and 876 J/m^2. With the difficulties involved in designing experimental methods for measuring pure Mode II fracture energy, it is often very difficult to measure G_{IIc} to an accuracy better than ±10%.

We can expect similar errors to occur in measurements of G_I and G_{II} in fatigue tests. At this stage there have been limited attempts to measure G_{IIIc} or to determine the error bounds on these measurements.

The effect that these experimental uncertainties have on growth will now be examined. From Tables 4 and 5, take as a first approximation n=4 for Mode II growth. Then the 10% uncertainty in G_{II} gives rise to 40% uncertainly in da/dN. This situation is similar in Mode I. Although the error in G_I is smaller, say 5%, the exponent n is larger, typically 8 (see Table 4). This makes the use of these growth laws, to predict fatigue life, very questionable.

An accurate prediction of delamination growth is very much dependent on the accuracy of measuring the values of delamination fracture energy during experiments. Furthermore, the scatter in the fatigue test data for composites gives rise to an additional uncertainty when it comes to applying this growth law in a service situation.

With the prevailing uncertainty in accurately measuring the value of Mode II delamination fracture energy, one questions whether it is worth putting any more effort into conducting extensive fatigue studies in order to predict delamination growth under cyclic loading.

The majority of the tests to date have concentrated on what was thought to be pure Mode I or Mode II growth. However, the growth of impact damage involves all three components. These conclusions are immediately apparent:

(a) A means of characterising Mode III growth is required.

(b) If the uncertainty in measuring G_{II} for a structural component cannot be overcome, then alternative ways of characterising the growth of delamination need to be considered.

3.3. Generalisation of the Growth Laws

There are two methods currently used to generalise the growth laws developed for pure Mode I or Mode II delamination growth. These approaches can be written as follows:

$$\frac{da}{dN} \approx cG^n \tag{2}$$

$$\frac{da}{dN} \approx f_1(G_I) + f_2(G_{II})$$

$$\approx \lambda_1 G_I^{n_1} + \lambda_2 G_{II}^{n_2} \tag{3}$$

where G is the total energy release rate with components G_I and G_{II} whilst n, n_1, n_2, λ_1, and λ_2 are experimentally determined constants. Equation (3) is empirical in nature and can be adjusted until it fits the data points for a series of Mode I and Mode II tests. Unfortunately it is entirely non-physical. It infers that the structure can subdivide the energy, i.e. G, available for crack growth into various components G_I and G_{II} and then

use these components in different ways. There is, therefore, a significant risk in using this approach in structures where growth is neither pure Mode I nor pure Mode II. Whilst equation (2) has a more physical interpretation, it must be remembered that G is really a vector quantity and does not equal $G_I + G_{II}$ unless growth is self-similar. We have also seen that the exponent n varies with the nature of the growth (see Table 4). For mixed-mode growth this infers that n will need to be separately determined. Indeed this cannot be totally achieved experimentally since for a general problem G cannot be measured from the movement of the load points. A combined experimental and finite element investigation is therefore needed for any particular problem and the need to account for irreversible effects, and perhaps even rate effects, in the matrix material needs to be evaluated.

3.4. Remarks

From a brief review of studies conducted to predicted delamination growth in composites under cyclic loading it can be seen that it is very difficult to predict delamination growth. Furthermore, due to inaccuracies involved in measuring the values of Mode II and Mode III delamination fracture energy, which in turn govern the delamination propagation under cyclic loading, current growth laws may be of little use under service conditions.

To aid in the development of a method for predicting the delamination growth in composites, the experiments conducted for this purpose should be aimed at:

(a) Minimising the errors involved in measuring the value of delamination fracture energy.

(b) A reduction in the scatter.

(c) Development of alternative approaches.

To date evaluation of the fracture energies has generally been performed assuming linear elasticity. However, the matrix material is known to be highly inelastic and to exhibit a strong rate dependence [4]. In Mode I there is a tendency for the fibre/matrix interface to fail thus limiting the effect of these non-linearities [4]. This is, in general, not true in Modes II and III, i.e. shear dominated failure, and may be one reason behind the large scatter seen in Mode II tests. (Shear rail tests to determine the shear stress/shear strain response of graphite epoxies reveals a behaviour similar to that for the bulk matrix material with extensive creep, stress relaxation, rate dependency and a large inelastic strain to failure even at room temperatures.) It is therefore highly desirable that current techniques be extended to allow for these effects.

4. RESIDUAL STRENGTH CALCULATION

There are several techniques available to predict the residual strength of an impact damaged composite. However, this report will focus on a generalised energy release rate approach.

The energy release rate approach: For Mode I self-similar crack growth of a through crack in the absence of body forces, the energy release rate G [54], can be written as:

$$T^* = \int_{\Gamma_{\varepsilon}\to 0} (W n_1 - t_i \frac{\partial u_i}{\partial x_1}) ds \tag{4}$$

where W is the energy density, Γ_ε is a vanishing small closed path around the tip, n_i is the component of a unit normal to the path in the x_i direction, t_i is the traction vector on the path Γ_ε defined as $t_i = n_j \sigma_{ij}$, and u_i is the component of displacement.
Here W is defined [55] as:

$$W = \frac{1}{2}\varepsilon_{kl} C_{ijkl} \varepsilon_{ij} - \beta_{ij}\varepsilon_{ij}(T - T_o) - \phi_{ij}\varepsilon_{ij}(M - M_o) + C_1(T, M) \tag{5}$$

where C_{ijkl} is the stiffness tensor, β_{ij} and ϕ_{ij} are related to the coefficients of thermal and moisture expansion and C_1 is a function of temperature and moisture. Let us now consider the integral J_s which we will define as:

$$J_s = \int_{\Gamma_s} W n_1 + t_i \frac{\partial u_i}{\partial x_1} ds \tag{6}$$

where Γ_s is the external boundary of the body. There is often a tendency to drop the subscript s and refer to J_s as J. Using Green's theorem it follows that:

$$G = J_s - \int_{V_s - V_\varepsilon} \left[\frac{1}{2}\varepsilon_{ij} \frac{\partial C_{ijkl}}{\partial x_1} \varepsilon_{kl} - \varepsilon_{ij} \frac{\partial}{\partial x_1}\left(\beta_{ij}(T - T_o) + \phi_{ij}(M - M_o)\right) + \frac{\partial C_1}{\partial x_1} \right] dV \tag{7}$$

where the integral of the second term in equation (7) is over the area between the two contours. Thus J_s will not equal the energy release rate G unless the area integral vanishes. At constant moisture and temperature J_s may be equal to G. However, in general the area integral will be non-zero and J_s, which is measured experimentally from the movement of the load points, [56] will not equal G.

In service aircraft heating is often localized and the moisture content varies. This will produce a spatial variation in the tensor C_{ijkl} with the result that the area integral will tend to be non-zero. Consequently when designing laboratory tests care should be taken to reproduce the near tip stress, strain, temperature and moisture fields rather than reproducing the 'global behaviour.' This is particularly true if the aim of the test is to establish such quantities as the critical damage size or the maximum permissible load.

For a three-dimensional fracture problem the integral on the right-hand side of equation (4) is no longer equal to the energy release rate and is referred to as T^* [54,56].

The application of this approach will be considered in section 6. It must be noted that, as mentioned in section 2, experimental tests and analytical studies have shown that for delaminations in (a) composite laminates, (b) at step lap joints, or (c) at mechanically fastened composite joints, a stage is reached after which a significant increase in the size of the damage does not significantly reduce the residual strength. This significantly simplified the methodology for estimating critical damage size and dramatically reduces the size of the required static strength test program.

Unlike the situation for fatigue life estimation, fracture mechanics based tools provide a useful tool in both understanding and predicting the static failure process. To further illustrate this, let us now consider the analytical solution for a circular disbond in an isotropic plate under remote hydrostatic compression [75].

4.1. Understanding Static Failure

When a composite material is subjected to impact, considerable damage can be caused since the cohesive strength of the plate through the thickness is very low and this in turn can lead to a deterioration in the strength of the plate. This failure process can be divided into two phases. In the first phase, the plate is impacted and the resulting response causes interlaminar separation. The size of this damaged area is a function of the impact parameters, impact energy, plate material, lay-up, etc. In the second phase, the damaged area spreads to the undamaged area through a combination of laminate buckling and further delamination.

In order for growth to occur, work of rupture is required. This energy must be available from either the work done by the compression forces (denoted by W) during the growth of the delamination, and/or from the decrease in the strain energy U of the system. Further delamination growth after the occurrence of buckling will depend on the magnitude of the fracture energy, Γ_o, which is defined as the energy required to produce a unit of new delamination area. If the energy release rate G at a given instance is greater than Γ_o, then further delamination growth will occur. To understand this process, consider a layered, isotropic circular plate containing a thin-film delamination of radius a as shown in Figure 1. The plate is subject to an in-plane compression until the load carried by the delaminated region reaches a critical value, at which buckling of this part of the structure occurs, leading to: (i) the onset of transverse deflections of the delaminated region; and (ii) reducing the amount of further load the delamination can support. This model is defined as "Specimen A" - see Figure 2(a).

The delaminated region will buckle when the stress it carries σ' reaches the critical buckling stress, σ'^*, for a clamped plate of radius a and thickness t [57], i.e., when:

$$\sigma' = \sigma'^* = \gamma^2 D / a^2 t \tag{8}$$

where $\gamma = 3.832$ and $D = Et^3/12(1-\nu^2)$. At this point, the externally applied stress is:

$$\sigma = \sigma^* = \sigma'^* \tag{9}$$

Prior to local buckling, the radial displacement at $r=b$ is:

$$u(b) = u_o(\sigma) = (1-\nu)\sigma b / E. \tag{10}$$

An analysis of the system energy release rate can be obtained [58] by using

$$G = \left(\frac{1}{2\pi a}\right)\frac{d(U-W)}{da} \tag{11}$$

At the initiation of local buckling, the applied stress σ^* and the displacement at the boundary of the plate is $u^*(b)$, where it can be shown [59] that:

$$u^*(b) = (1-\nu)\sigma^* b / E \tag{12}$$

After buckling, the stiffness of the delamination decreases from $E' = E$ to $E' = \bar{\lambda}\, E$, where $\bar{\lambda}$ is given by [58] as:

$$\bar{\lambda} = (1 + 1.207(1+\nu))^{-1} \tag{13}$$

Because the delamination loses some of its stiffness due to buckling, this causes the compliance of the disk $r \in [0,a]$ to increase. This can be simply modelled as a plate under compression, with an inner section having Young's modulus E_i ($<E$) and an outer section of modulus E as shown in Figure 2, "Specimen B."

For these two specimens to be equivalent, we require the displacements at $r=a$ to be equal, i.e.:

$$u_A(a)=u_B(a), \tag{14}$$

where $u_A(a)$ is the displacement at $r=a$ for specimen A and from [59],

$$u_A(a)=\left[(1-\nu)\sigma_i a/E\right]\left[1-(t/T)(1-\bar{\lambda})\right]^{-1} \tag{15}$$

and, for specimen B

$$u_B(a)=(1-\nu)\sigma_i a/E_i. \tag{16}$$

Here $u_A(a)$ was obtained from the requirement that

$$\sigma_i=(t/T)\sigma_{i1}+((T-t)/T)\sigma_{i2} \tag{17}$$

and

$$u_{A1}(a)=u_{A2}(a) \tag{18}$$

where

$$u_{A1}(a)=(1-\nu)\sigma_{i1}a/E' \tag{19}$$

and

$$u_{A2}(a)=(1-\nu)\sigma_{i2}a/E. \tag{20}$$

In the above, $u_{A1}(a)$ and σ_{i1} are the displacement and stress at $r=a$ of region 1 in specimen A where regions 1 and 2 are defined in Figure 2(a). From equation (14) we find that:

$$E_i=\lambda E=(1-(t/T)(1-\bar{\lambda}))E. \tag{21}$$

For specimen B, the displacement at any point $\in[a,b]$ is given by [59]:

$$\begin{aligned} u(r)=&-(a^2b^2/b^2-a^2)\\ &\times\{(-1/r)(\sigma-\sigma_i)(1+\nu)\\ &+r(\sigma_i/b^2-\sigma/a^2)(1-\nu)\}/E \end{aligned} \tag{22}$$

To find the displacement at the boundary $r=b$ of specimen B, we require the inner displacement (at $r=a$) between regions 1 and 2 to be continuous,

$$u_{B1}(a)=u_{B2}(a), \tag{23}$$

where u_{B1} and u_{B2} are given by equations (16) and (22). Solving equation (23) yields:

$$\sigma_i=\sigma[1+ec]^{-1}, \tag{24}$$

where

$$e=(1-\lambda)/\lambda,\ c=\frac{1}{2}(1-\nu)(b^2-a^2)/b^2 \tag{25a,b}$$

Substituting for σ_i into equation (22) yields:

$$u(b)=u_o(\sigma)[1+\Theta], \tag{26}$$

where

$$\Theta = 2ea^2(2b^2 + e(1-\nu)(b^2 - a^2))^{-1}. \tag{27}$$

Thus the displacement undergone since buckling is:

$$u_p(b) = (1-\nu)(\sigma - \sigma^*)b[1+\Theta]/E \tag{28}$$

and the total displacement is given by:

$$u(b) = u^*(b) + u_p(b)$$

$$= u_o(\sigma)[1 + (1 - \sigma^*/\sigma)\Theta]. \tag{29}$$

Because of buckling, not only does the compliance of the inner disk $r \in [0,a]$ increase, but also that of the whole specimen. As a result of this, the load-displacement curve is no longer linear, but in fact bi-linear. (A typical load-displacement curve is shown in Figure 3.)

With these assumptions it follows that:

$$G = (1-\bar{\lambda})(1-\nu)t(\sigma^2 - \sigma^{*2} + m^2(\sigma - \sigma^*)^2)/E(1+ec), \tag{30}$$

where

$$m = e(1-\nu)a^2(2b^2 + e(b^2 - a^2)(1-\nu))^{-1} \tag{31}$$

Now ec and m are of the orders (t/T) and (ta^2/Tb^2) respectively, thus for (t/T) small, equation (30) can be approximated by:

$$G = (1-\bar{\lambda})(1-\nu)t(\sigma^2 - \sigma^{*2})/E, \tag{32}$$

Plots of G as a function of the delamination radius a and the load P for a specimen of dimensions b=75 mm, T=3.1 mm, t=0.5 mm and modulus E=68.9 GPa and ν=0.3 are shown in Figures 4 and 5.

In order to generalise the energy release rate for arbitrary parameters and fracture energy Γ_o, we introduce the following normalizations:

$$\Gamma_o = \Gamma_o E/(1-\bar{\lambda})(1-\nu)t, \tag{33}$$

$$\sigma = \sigma/\bar{\Gamma}_o^{1/2}, \tag{34}$$

$$\bar{a}^2 = a^2 t\bar{\Gamma}_o^{1/2}/\gamma^2 D. \tag{35}$$

With this notation equation (32) can be rewritten as:

$$G/\Gamma_o = (\bar{\sigma}^2 - 1/\bar{a}^4), \tag{36}$$

This solution reveals that as the size of the delamination increases, the energy release rate, and hence the residual strength, tends to an asymptotic value. This phenomena plays a central role in the damage tolerance assessment of impact damage, and is frequently observed in residual strength tests on impact damaged structural components, see sections 2 and 4.

4.1.1. Finite Element Analysis

Before performing a detailed finite element analysis of an impact damaged structure it is first necessary to establish that the analysis technique is capable of reproducing known analytical solutions. The problem described above represents one such potential solution. Let us consider the specific case when the structure is a symmetrically delaminated specimen with thickness $2T$, having dimensions b=75 mm, T=3.1 mm, t=0.5 mm, and modulus E=68.9 GPa and ν=0.3.

Due to symmetry it was only necessary to model half of the specimen. The finite element mesh is shown in Figure 6. This mesh was generated using four-noded axisymmetric elements. Due to concern about the adequacy of four-noded elements to model the bending that occurs when the delamination buckles, another mesh was created, similar to the one above, except that the delaminated layer is now composed of eight-noded elements.

Four delamination radii a=15, 20, 35 and 45 mm were considered, and analyses were conducted to determine:

(i) the energy release rate as a function of applied load;

(ii) the energy release rate as a function of delamination radius.

In each case the stress intensity factor and hence G was calculated from the resultant opening of the faces of the crack.

The resultant values of G are shown in Figures 7 and 8, as a function of applied load and radius of the delamination, together with the corresponding analytical values. From these figures it can be seen that the closed form analytical solution for G agrees quite well with the finite element solution, obtained using eight noded elements.

4.1.2. Remarks

A simple closed form solution for the energy release rate G has been obtained for a circular delamination in a circular plate and was verified by means of finite element analysis. This solution reveals the dependence of G on the geometry and location of the delamination. It may also be useful as a "benchmark" test for evaluating the ability of various finite element packages to model delamination damage.

It is important to note that as the size of the delamination increases, G tends to an asymptotic limit. This is consistent with observed experimental results for which the residual strength asymptotes to a lower bound as the size of the impact damage increases.

5. APPLICATION OF THE T* INTEGRAL TO PREDICTING RESIDUAL STRENGTH

5.1. The Finite Element Model

Let us now turn to the problem of a laminated composite structure containing an internal delamination. Details of the finite element mesh used in this work are shown in Figure 9. It is a model of an impact damaged laminate with a fastener hole under compression. The dimensions of the model are the same as those used in the experimental work of [35]. The specimen tested as a $[0/45/0_2/-45/0_2/45/0_2/-45/0]_s$ T300/5208 graphite-epoxy

laminate and contained a centrally located hole of 9.5 mm diameter, surrounded by delamination damage due to impact and poor drilling.

The elements used are mostly twenty-noded iso-parametric elements with directionally reduced integration and 2x2x3 Gaussian quadrature points, with the 3 points being taken through the ply thickness. Detailed description of the reduced integration scheme can be found in [60]. The crack tip elements along the circular delamination are fifteen-noded iso-parametric wedge elements. The effect of moving the relevant mid-side nodes of these elements to the quarter point positions to simulate the desired singularity is investigated. Solutions with and without quarter point shifts are compared.

The initial damage around the fastener hole from [35] is modelled as a circular delamination of radius 13.75 mm between the second and third plies (i.e. between the 45° and 0° plies). This is an approximate simulation of the initial damage as shown in Figure 10(a). It can be seen from the ultrasonic C-scan that the initial delamination is nearly circular.

The two plies above and below the delamination are modelled separately with ordinary three dimensional elements while the remaining 20 plies are modelled with super-elements with displacements varying quadratically in the local iso-parametric coordinate system. The material properties used are those of Narmco-Thornel T300/5208 and are tabulated in Table 6. The effect of changing the value of the shear modulus G_{23} is investigated. In the first case, the value of G_{23} is taken as equal to that of G_{12} and G_{13}. In the second case, G_{23} is estimated via the approximation:

$$G_{23} = E_{22} / 2(1+\nu_{23}) \tag{37}$$

which was also used in [61]. The properties of the matrix material are given in Table 6.

It is important that in the finite element model, the faces of the delamination are prevented from overlapping. Otherwise, non-physical solutions may be obtained. By examining the solutions of the displacements, it is found that some parts of the delaminated faces have overlapped. Thus a series of constraint equations are applied to appropriate nodes to simulate local closure. The effect of correctly restraining the delamination faces is also studied, with three sets of solutions involving: (i) incorrect restraints, (ii) correct restraints, and (iii) no applied restraints. A compressive strain of 0.006 is applied at the ends of the model. This value of strain represents the experimentally measured, far-field failure strain for this specimen, see [35].

5.2. Results and Discussion

An interesting characteristic of the distribution of T^*, in this particular problem, is the existence of three peaks along the circular delamination front, see Figure 11. The T^* distribution has the largest peak located at θ=60°, where θ is defined in Figure 9. The value of T^*_{max} for the correct restraint condition is 70.8 Jm^{-2}. This value compares favourably with the G_{Ic} value of 76 Jm^{-2} for neat 5208 Narmco resin obtained by Bascom *et al.* [62]. Double cantilever Mode I tests provide values of 78-88 Jm^{-2} for the G_{Ic} of the T300/5208 material system [17,18].

It must be mentioned that the value of T^*_{max} is very sensitive to the restraint condition applied to the delamination faces in order to prevent overlapping of the surfaces[48]. Incorrect conditions result in an 11% error in T^*.

The influence of shear moduli is also shown to be significant, particularly in the distribution of T^*. This effect is important since the value of G_{23} used in the numerical simulation affects the calculation of interlaminar shear stresses crucial in the determination of delamination behaviour. In Figure 12 it can be seen that although the basic shape of the distribution of T^* remains quite the same, the relative and absolute magnitude of the peaks are greatly affected. The two cases considered are perhaps extreme cases since the true or effective value of G_{23} may lie somewhere in between the values used in cases *A* and *B*.

When quarter point shifts of the crack tip nodes are not performed the distribution of T^* is changed remarkably (see Figure 13). In this case the analysis failed to detect the secondary peak at θ=45°. These results clearly illustrate the importance of correctly modelling the stress singularity and the need to prevent overlapping of the delamination faces.

Figure 10b shows the c-scan of the final shape and size of the damage after 20,000 cycles. It can be seen that the points of maximum growth coincide with the local maxima of T^*. Furthermore, as mentioned earlier, the predicted value of T^*_{max}= 70.8 Jm^{-2}, at the failure load, compared well with G_{Ic} for the material.

The results of this analysis suggests that:

1. The T^* criteria is a useful tool for evaluating the residual strength of damaged components.
2. Better experimental methods are needed in order to determine more accurately important orthotropic laminate properties such as the interlaminar shear moduli [63]. Presently, some properties, such as G_{23}, are difficult to determine experimentally and are prone to experimental errors.
3. More accurate and consistent methods of obtaining mixed mode energy release rates are needed. These values would aid in a more accurate and consistent determination of failure loads.
4. In numerical analyses, accurate determination of crack tip element stresses is important. The use of quarter point shifts to simulate the stress singularity should not be ignored, see [64] for more details.
5. The effects of local crack closure (i.e., the closure of delamination faces) on the values of T^* are important; care must be taken in finite element analyses to avoid non-physical solutions through the use of appropriate restraints, see [64] for more details.
6. Unlike cracks in metallic structures bi-axial stress states may have a very significant effect on the critical fracture (failure) load. This will be investigated in more detail in section 7.

6. EFFECT OF ANISOTROPIC PLASTICITY

With the development of tougher matrix materials such as PEEK the influence of plasticity on the structural integrity of composite components has become more important. The spread of plasticity and the plastic zone size in the vicinity of the crack-tip region are of interest since it may be adequate to employ fracture mechanics

techniques if the extent of plasticity is small. At present, data for the plastic stress-strain behaviour of composite materials are not readily available. Another problem lies in the definition of equivalent stress and strain. In this work, the classical theory of anisotropic plasticity is used, together with a reduced equivalent stress-strain curve experimentally determined by Chen and Sun [65]. In this section an incremental finite-element analysis is performed for a three-dimensional impact delamination problem and the effect of plasticity on the fracture parameter T^* is investigated.

In the case of incremental plasticity, the value of T^* at the end of a load sequence 0, $P_1,...P_N$ is given by

$$T^* = \sum_{i=1}^{N} \Delta T^* \tag{38}$$

where ΔT^* is given by

$$\Delta T^* = \lim_{\varepsilon \to 0} \int_{\Gamma_\varepsilon} \left(\Delta W n_1 - \Delta \left(t_i \frac{\partial u_i}{\partial x_1} \right) \right) ds \tag{39}$$

and for iso-thermal and iso-moisture problems the energy density W is

$$W = \int \sigma_{ij} d\varepsilon_{ij} \tag{40}$$

6.1. Anisotropic Plasticity

This work uses the classical three-dimensional anisotropic theory of plasticity first established by Hill. The criterion for yielding is expressed by the 'plastic potential' defined as

$$2f = (\alpha_T - \frac{1}{2}\alpha_L)(\sigma_{22} - \sigma_{33})^2 + \frac{1}{2}\alpha_L(\sigma_{33} - \sigma_{11})^2 + \frac{1}{2}\alpha_L(\sigma_{11} - \sigma_{22})^2 + \alpha_S(\gamma_{12}^2 + \gamma_{23}^2 + \gamma_{31}^2) \tag{41}$$

where

$$\alpha_L = \frac{1}{X^2},\ \alpha_T = \frac{1}{Y^2},\ \alpha_s = \frac{1}{T^2} \tag{42}$$

X, Y are the tensile yield stresses in the fibre and transverse directions, and T is the shear yield stress.
Clearly, in the isotropic case, when X=Y and $T = Y/\sqrt{3}$, equation (41) reduces to the familiar von Mises yield criterion

$$2f = \frac{1}{2}\alpha_T \left[(\sigma_{22} - \sigma_{33})^2 + (\sigma_{33} - \sigma_{11})^2 + (\sigma_{11} - \sigma_{22})^2 + 6(\gamma_{12}^2 + \gamma_{23}^2 + \gamma_{31}^2) \right] \tag{43}$$

Yielding is considered to have occurred when the stress state is such that $2f$=1. In classical incremental plasticity theory, the plastic strains are defined as:

$$d\varepsilon_{ij}^p = \frac{\partial f}{\partial \sigma_{ij}} d\lambda \tag{44}$$

where $d\lambda$ is a constant of proportionality to be determined. Carrying out the above differentiations, we obtain the Prandtl-Reuss equations

$$d\varepsilon_{11}^p = (\alpha_L \sigma_{11} - \frac{1}{2}\alpha_L(\sigma_{22} - \sigma_{33}))d\lambda$$
$$d\varepsilon_{22}^p = (\alpha_T(\sigma_{22} - \sigma_{33}) - \frac{1}{2}\alpha_L(\sigma_{11} - \sigma_{33}))d\lambda$$
$$d\varepsilon_{33}^p = (\alpha_T(\sigma_{33} - \sigma_{22}) - \frac{1}{2}\alpha_L(\sigma_{11} - \sigma_{22}))d\lambda \qquad (45)$$

$$d\varepsilon_{12}^p = \alpha_s \gamma_{12} d\lambda$$
$$d\varepsilon_{23}^p = \alpha_s \gamma_{23} d\lambda$$
$$d\varepsilon_{31}^p = \alpha_s \gamma_{31} d\lambda$$

We define the equivalent stress $\bar{\sigma}$ after Hill:

$$\bar{\sigma} = \sqrt{\frac{3}{2}\frac{2f}{(\alpha_Y + \frac{1}{2}\alpha_L)}} \qquad (46)$$

To evaluate the constant dλ we define the plastic work done as

$$dW^p = \bar{\sigma}\, d\bar{\varepsilon}^p \qquad (47)$$

where $d\bar{\varepsilon}^p$ is the equivalent plastic strain increment. It should be noted that equation (47) is the basic definition for $d\bar{\varepsilon}^p$, once $\bar{\sigma}$ is defined. Another way of expressing the incremental plastic work is

$$dW^p = \sigma_{ij}\, d\varepsilon_{ij}^p \qquad (48)$$

Substituting equation (45) into equation (48) it is easily shown that

$$dW^p = \sigma f\, d\lambda \qquad (49)$$

From equation (46) we see that

$$2f = \frac{2}{3}\left(a_T + \frac{1}{2}a_L\right)\bar{\sigma}^2 \qquad (50)$$

and substituting this into equation (49) we have

$$dW^p = \frac{2}{3}\left(a_T + \frac{1}{2}a_L\right)\bar{\sigma}^2 d\lambda \qquad (51)$$

Equating equation (51) with equation (47) we obtain

$$d\lambda = \left(\frac{3}{2a_T + a_L}\right)\frac{d\bar{\varepsilon}^p}{\bar{\sigma}} \qquad (52)$$

Equations (45), (46) and (52) completely define the orthotropic plasticity flow rule used in this work. It should be noted that $d\bar{\varepsilon}^p$ is estimated by the program from the given equivalent stress-strain curve and the strain components calculated using equation (45).

At yield, $2f$=1 by definition, if we substitute the values X=1500MPa and Y=60MPa into equation (46) we obtain a value for the equivalent yield stress

$$\bar{\sigma}_Y = 73.45\,MPa \qquad (53)$$

This value of equivalent stress represents the limit of the linear or elastic portion of the stress-strain curve. It should be noted that the value of X used is the ultimate failure stress of the composite in the fibre direction, since it may be assumed that negligible yielding occurs in this direction prior to failure. Hence it is clear that the parameter $\bar{\sigma}_Y$ is significantly affected only by Y, the yield stress across the fibre direction. This emphasises the assumption that plasticity effects are predominantly dependent upon the behaviour of the matrix material.

For the nonlinear part of the equivalent stress-strain curve, data from work by Chen and Sun [65] are used. The relationship was obtained by fitting a curve through experimental data. If $\bar{\sigma}$ is expressed in MPa, the relationship is

$$\bar{\varepsilon} = (7.107 \times 10^{-11})(\bar{\sigma})^{3.7} \tag{54}$$

Substituting equation (53) into equation (54), the equivalent yield strain can be obtained:

$$\bar{\varepsilon}_Y = 5.6997 \times 10^{-4} \tag{55}$$

An equivalent elastic modulus may thus be defined:

$$\bar{E} = \frac{\bar{\sigma}_Y}{\bar{\varepsilon}_Y} = 128.86 GPa \tag{56}$$

We assume 'yielding' to have occurred when the equivalent stress-strain behaviour surpasses the linear or elastic region of the curve. Another assumption used in this work is that no account is taken for the possibility that the yield stress in the across-the-fibre direction may be different in compression than in tension. Furthermore, due to the lack of data on shear yield stresses, the shear yield stress used here is assumed to be

$$T = \frac{Y}{\sqrt{3}} \tag{57}$$

although in general this need not necessarily be so.

6.2. Result and Discussion

The applied load was increased in 10 increments until the spread of plasticity was found to be extensive. It should be noted, however, that 'plasticity' for graphite-epoxy composites is unlike plasticity as traditionally understood for metals in that, for the former, there is usually no clearly defined yield point. In our simulation, a linear region in the stress-strain curve has been artificially imposed. Nevertheless, this does not invalidate the analysis since the object of the analysis is to determine whether plasticity causes a significant difference in the behaviour of T^*.

Figure 14 shows the distribution of the ratio $T^*_{plastic}/T^*_{elastic}$, i.e. the elastic value of T^*, and its variation along the delamination front with loading increment. The maximum value of T^* is only slightly altered with increasing plasticity. The maximum value of the ratio $T^*_{plastic}/T^*_{elastic}$ is given in Table 8. Significant plasticity begins to appear at load increment 4 (40% of total applied load) and it is after this stage that the deviations in T^* begin to become apparent (see Figure 14). There are differences of up to 50% for some positions along the delamination front, although at points of maximum T^* (i.e. at points A and C in Figure 14) the deviations from the elastic solutions are very small. A point of particular interest is at B, where with increasing plasticity, T^* changes sign from positive to negative. In other studies, this behaviour has been associated with local load-shedding [66]. It should be noted here that the delamination surface restraints applied to the model

remain the same throughout the loading increments. These restraints are obtained from a previous elastic run. To be strictly correct, however, the delaminated surfaces should be checked for local crack closure for each loading increment and the solution reiterated. At present, such a procedure is unfortunately too time-consuming and costly. It is also found that the deviations of T^* are primarily due to the traction terms of the integral.

It appears that the first elements to become plastic belong to the second layer (i.e. the 45° layer) and that plasticity originates from the delamination front. After load increment number 3 the plasticity spreads in directions ±45° to the global loading direction. It readily penetrates the 0° layers above and below the second layer during and after load increment 4, suggesting that the spread of plasticity through the thickness of composite laminates may not be significantly restrained by the ply configuration.

The results of this work indicate that:

1. Plasticity may not significantly affect the severity of the damage, since it does not contribute to significant deviations in T^*_{max} and the strain energy density factor [67]. This implies that for at least some cases, a full-scale plasticity analysis is not necessary and therefore significant cost in computing time can be saved. For the problem investigated here the full plasticity solution required more than six times the CPU time of the elastic static analysis.
2. The T^*-integral applied to composite plasticity may become negative with increasing plasticity. It is believed that this phenomenon may be caused by local load-shedding, see [66].
3. It is shown that matrix plasticity can readily spread into adjacent layers of different ply orientations and is not necessarily restrained from spreading through the thickness.

For metals, crack-tip plasticity can be accounted for by replacing the crack length a by an effective length $a+rp$ where rp is related to the size of the plastic zone. If this approach is adopted for the present problem, then it is known that once a characteristic damage size has been exceeded the crack-tip parameters are invariant to size [1], and this would suggest that the parameters should be insensitive to matrix ductility. The present work appears to confirm this hypothesis. The invariance of the governing fracture parameters to plasticity should also hold for other problems for which the governing crack-tip parameters asymptote to a constant value as the size of the crack increases, see [67] for more details.

7. IMPLICATIONS FOR FIBRE COMPOSITE REPAIRS

Having gained an understanding of the mechanisms governing the behaviour of impact damaged composites let us now consider its implications for repair. In this section attention is focused on the behaviour of impact damage, under both uniaxial and bi-axial compressive loading, and a simple repair methodology is developed. This methodology is then verified via a simple coupon test program and subsequently by a repair to an impact damaged F/A-18 Horizontal Stabilator.

There are two possible methods for repair impact damage. One approach is to remove the damage region and use an internally bonded repair. This is very effective, but

requires extensive bonding facilities resulting in a significant period of non-utilization of the component. An alternative approach is to increase the strength by reducing the net sectional stresses. This can be achieved by placing an external patch over the damaged area.

In this section the T^* is applied to the problem of an impact damaged composite structure repaired with an externally bonded patch. A simple design methodology is presented and substantiated via a laboratory test program [68]. This methodology is further illustrated by a repair to a damaged horizontal stabilator which is tested to ultimate load.

7.1. Numerical Analysis of Bonded Repairs

In order to understand the mechanisms governing failure and the increase in residual strength of a repaired structures, which contains impact damage, a detailed three-dimensional finite element analysis of the problem outlined in section 5.1 was undertaken. The initial damage around the fastener hole, of 9.5mm diameter, was modelled as a circular delamination of 13.75 mm radius between the second and third plies (i.e. between the 45° and 0° plies). This is an approximate simulation of the initial damage where it was found, from ultrasonic C-scanning, that the initial delamination was nearly circular, see section 5.1. A compressive load of 150 kN was applied to the ends of the model in the x-direction (see Figure 9).

To investigate the use of an externally bound repair a 12 ply $(0/+45/0_2/-45/0)_s$ laminate bonded over the damaged area was analysed. This patch contained a hole to allow for the possible insertion of a fastener. To evaluate fastener/structure interaction effects various boundary conditions were applied to the hole. These were chosen to represent: 1) an open hole, 2) an interference fit fastener and 3) a bonded insert.

7.1.1. Results and Discussion

For each configuration the value of the crack tip energy integral T^* was computed at each node around the crack tip. A summary of the maximum values of T^* is given in Table 9. The angles at which the respective maxima occur, which are referred to as θ_T, are also shown.

It was observed that the two plies above the delamination moved out of plane, i.e. crack opening and/or closure. For all of the cases analysed this out of plane movement was non-symmetric. This asymmetry results in the asymmetric growth of the delamination which is consistent with the C-scans and thermal emission measurements [35]. The results of this analysis suggested that:

1. When the patch material has the same stiffness as the parent laminate the reductions in T^* can be estimated (see Table 9) by multiplying the values corresponding to the unrepaired structure with the square of the reduction in the net sectional stress, see [69] for more details. This infers that the residual strength of a repaired structural component can be estimated by the following simple formulae:

$$\frac{\text{Residual Strength}(\textit{repaired})}{\text{Residual Strength}(\textit{unrepaired})} = \frac{\sigma(\textit{unrepaired})}{\sigma(\textit{repaired})} \qquad (58)$$

2. Prohibiting local bending at the hole had an insignificant effect on the fracture parameter. However, prohibiting in-plane movement and local bending reduced T^*. This reduction in T^* would correspond to an increase in the failure load of between 11% to 16%. As a result, experimental results, using either a bonded or an interference fit insert to simulate this level of local restraint, are required to evaluate this effect further.

3. Load bi-axiality has a marked effect of the fracture parameter and hence on the failure of the structure.

7.2. Experimental Program

7.2.1. Specimen Fabrication

To confirm this prediction a coupon test program was undertaken. The graphite epoxy material used throughout these tests was AS4/3501-6 with a ply configuration of $[(+45_2/-45_2/0_4)_3/90]_s$. Before the specimens were cut from these panels, they were C-scanned to determine the void content of the material.

Each specimen was impacted with a 12mm (1/2") diameter ball bearing with a mass of 1 kg and from a height of 1.3m. A summary of the absorbed energies is listed in Table 10. The extent of damage was limited by the use of 20, 30 and 40mm "windows" clamped around the specimen during the impacting. For the single impact specimens all three diameter "windows" were used to produce damage with diameters ranging from approximately 19.8mm to 39.7mm. A 6mm diameter hole was also drilled through the centre of the damaged region of these specimens. All specimens were subjected to a C-scan of the impacted area and the damage size was approximated from these scans. A more detailed description is given in reference [68].

7.2.2. Repair Fabrication

In order to validate the simple design rule previously postulated, it was required that the effective stiffness and ply configuration of the patch be representative of the parent material. The material used for the patch was AS4/3501-6 and was 16 plies thick, with a ply configuration of $[0_2/+45/-45/-45/+45/0_2]_s$. The ends of the patch were scarfed to reduce the peel stresses in the adhesive, see [68]. The length of the patch and distance to the edge of the grips were 190mm and 60mm, respectively. The patches were bonded to the parent laminate using the cold setting acrylic adhesive FLEXON 241. This adhesive was chosen for its excellent shear strength, ease of application and because environmental effects were not an issue in this test series.

7.2.3. Test Methodology

Unrepaired specimens were tested individually while repaired specimens were tested back-to-back [68]. Four strain gauges were bonded on the unrepaired specimen; two above and two below the damage. Each pair was positioned on the mid-width and on opposite faces in order to determine axial and bending strains. The repaired specimen only had two strain gauges located on the patched side. In each case the gauges were 110mm from the centre of the specimen. The specimens were loaded in compression and to avoid the problem of global buckling an anti-buckling rig was used [68].

7.2.4. Results and Discussion

All specimens, except two which exhibited extensive bending, produced load versus strain curves which were essentially linear to failure. Specimens 4 and 5 exhibited extensive bending near, and up, to failure thereby reducing the failure load obtained. The failure strains for each specimen are tabulated in Table 10. These results show that the failure strains follow the asymptotic nature outlined in section 2. The variation in the failure strains, for a given damage size, reflects variations in specimen geometry as well as variations in the structure of the internal damage due to impact. In all cases, the patches and the adhesive bond failed after the parent laminate.

The failure load of the repaired specimen can also be predicted (see Table 10) using equation (58) and only requires a knowledge of the unrepaired residual strength and the change in net sectional stresses due to patching. The change in the net sectional stress can be calculated directly from the change in net sectional area. This result is believed to substantiate the trends predicted in the previous section and significantly simplifies the repair design philosophy.

8. DAMAGED ASSESSMENT OF AN F/A-18 HORIZONTAL STABILATOR

8.1. Background

As an example of how this approach can be used to repair damaged structural components let us consider the repair of a damaged F/A-18 horizontal stabilator, which has recently been incorporated into the Composite Repair Engineering Development Program (CREDP). CREDP is a joint program between the Canadian Forces (CF), the RAAF and the United States Navy (USN) to evaluate the repair capability of damaged composite components on the F/A-18. As part of the CREDP program, the Aeronautical Research Laboratory (ARL) was tasked to develop and analyse a repair for a damaged horizontal stabilator, which was initially classed as unserviceable and irreparable due to two fragment strikes from a tracer rocket.

The F/A-18 horizontal stabilator comprises an aluminium honeycomb sandwich structure with graphite/epoxy skins, with fibres oriented in the 0° and $\pm 45^\circ$ directions. The cross-section of the stabilator is fully symmetric. In the region of the damage the skin is 29 plies thick (3.68mm), but tapers off to 7 plies (0.89mm) at the leading edge and has incurred extensive local damage to the composite skin and underlying honeycomb, but neither fragment penetrated to the other side of the stabilator. As shown in Figure 15, the two damaged areas are approximately the same size; however there was a slight difference in the impact angle of the two fragment strikes. The location of the damaged zone and ply orientation can be seen in Figure 16.

8.2. Structural Evaluation

In order to evaluate the structural significance of the damage, i.e. if the original design was optimised for impact damage, a test rig capable of applying the design loads was used. The stabilator was mounted in the rig by means of the spindle, which is used to connect the stabilator to the aircraft. Hence all bending loads applied to the stabilator are transferred to the rig via the spindle. A lever arm connected to the root of the stabilator transfers all the torque loads to the test rig. Static loads were applied to the structure via

two flexible air bags. The design of the test rig is such that it allows these air bags to be mounted above or below the test article, as described in reference [70].

Four strain gauge rosettes were located in a rectangular pattern around the damage zone and in the corresponding location on the undamaged skin, see Figure 16. The gauges in each rosette were aligned in the direction of the 0° and $\pm 45^\circ$ fibres. Two displacement transducers were placed halfway between the left hand inboard rosettes (1 and 2), in the 0° fibre direction, as seen in Figure 16. The gauge length of the displacement transducers was 385mm. The strain gauge rosettes and displacement transducers were positioned so as to evaluate the change in compliance of the structure due to the damage.

Displacement and pressure transducers were required to measure the extension and pressure of each air bag. The force applied by each air bag is a function of these two variables and was determined from a calibration graph. The root bending moment (RBM) was calculated and used as the reference load applied to the structure. Three extra displacement transducers were attached to the stabilator at the tip, leading and trailing edges, to measure tip displacement and torque induced by the applied load.

8.2.1. Test Description

The first stage of the investigation involved the application of a static load by incrementing the air bag pressure in steps of 10 kPa. Here the maximum load applied to the structure was not considered to be critical since the primary objective was a comparison between the strains and the compliance on the top and bottom surfaces of the stabilator. Initially, the air bags were placed underneath the stabilator, producing tension in the damaged surface skin, and a dummy loading and unloading run was performed to allow the structure to settle. Several loading and unloading runs were made in this configuration with strain gauge and transducer readings being conducted at each increment of pressure. The loading was then repeated with the air bags re-configured above the stabilator producing a compressive load in the damaged surface.

8.2.2. Results and Discussion

The Ultimate Bending Moment (UBM) and the Design Limit Bending Moment (DLBM) for the horizontal stabilator are 120.3 kNm (1065 kip-in) and 80.2 kNm (710 kip-in), respectively [70]. The RBM was calculated for each load step and the test achieved 31% (47%) and 26% (39%) of the UBM (DLBM) in tension and compression, respectively.

The strain survey results for one loading cycle are shown in Table 11, for the case when a compressive load was applied to the damaged surface. The results for the case of tensile loads applied to the damaged surface are very similar. All strain values are presented in microstrain. Table 11 shows that there was no structurally significant difference between the strain gauge results for strains in the 0° fibre direction on the top (damaged) and the bottom (undamaged) surfaces, except for gauge D2 which has a 24% to 27% reduction depending upon the value of the RBM, due to damage. This may be due to the gauge being shielded by the damage. The compliance readings, tabulated at the bottom of the tables as 'U' for the undamaged surface strain and 'D' for the damage surface strain, show no significant difference between the top and bottom surfaces. This implies that the global compliance has not been affected by the damage and indicates that there is little structural degradation. This was confirmed by a thermal elastic evaluation of the damaged region, see [71].

8.3. The Finite Element Model

To understand the mechanisms involved in this problem and to assist in designing a repair a finite element analysis was undertaken. The damage section of the horizontal stabilator was modelled by representing the skin as a two-dimensional membrane with effective laminate properties and the underlying honeycomb as three-dimensional iso-parametric brick elements. The small changes in the compliance and the local strains due to damage, as observed in the previous section, suggest the possibility of using an external doubler to repair the damaged stabilator. In this case the adhesive layer was modelled using three-dimensional iso-parametric brick elements with the doubler represented by two-dimensional membrane elements, with an effective laminate property. Three cases were analysed, the undamaged skin, the damaged but unrepaired skin and the damaged and repaired skin. The damaged, but unrepaired, model contained 520 nodes, 128 elements and 1255 degrees of freedom and the repaired model contained 818 nodes, 256 elements and 1976 degrees of freedom.

The material used for the skin and the doubler was again AS4/3501-6 and the associated laminate properties can be found in Table 12. Young's modulus of the honeycomb and the adhesive was taken to be 2.0 GPa and 1.8 GPa, respectively, with a Poisson's ratio of 0.35 for both. The doubler was 16 plies (2.032 mm) thick and a pressure of 400 MPa was applied along one edge of the skin.

The accuracy of the finite element model was evaluated by comparing the predicted and measured strains, obtained in [70,72]. For the undamaged stabilator the ultimate design bending moment corresponds to a design limit strain ε_{dl}, of approximately 4850 $\mu\varepsilon$, see [70,72]. The corresponding predicted strains at the two trailing edge strain gauges, 1 and 3, were approximately 4950 $\mu\varepsilon$ and 4860 $\mu\varepsilon$, respectively, and the predicted value of strain over the region measured by the LVDT was also close to the measured value. However, because the actual structure tapers off towards the leading edge, the strains in the numerical model closest to the leading edge (gauges 2 and 4) were higher than those achieved in the experiment. Nevertheless it was felt that this model would be useful in predicting the change in strain due to the application of an external doubler.

8.3.1. Predicted Reduction in Strain Due to an External Doubler

Following the development of the undamaged finite element model, two cases were considered. The first case simulated the damaged, but unrepaired, stabilator and the second case modelled a bonded external doubler. A summary of the predicted strains measured by the LVDT and the strains, in the 0^{o} fibre direction, at gauges 1-4 are given in Table 13.

The application of the external doubler significantly reduced the strain around the damaged zone leading to an average reduction in strain of 28.5%. The peak adhesive shear stress was less than 25 MPa and was below the endurance level of the thin film adhesive FM73, see [73], indicating that the repair should not debond and should be inherently damage tolerant, see [73]. The stress concentration around the damage was also found to be very localised and was consistent with the experimentally measured thermal emission profile [72], as well as with the experimentally measured values of strain and compliance.

8.4. Repair Evaluation

Following the initial tests on the horizontal stabilator the damaged region was repaired using an external doubler which was tailored to matched the stiffness of the stabilator skin. The ply configuration of the repaired laminate was $(+45/-45/0_2/90/-45/+45/0)_s$. The loose fibres around the impact zone were removed and the edges of the damage zone were scarfed. The whole region was then filled with packing adhesive and the repair laminate was then bonded onto this surface using FM73 adhesive.

The test procedure, outlined in section 8.2.1, was then repeated with additional strain gauge rosettes placed on the repair. The location of the repair ranged from 0.610m (24") to 1.092m (43") from the root of the stabilator. The repair successfully withstood both tension and compression loading, see [74]. In tension, the majority of the region exceeded the DLBM. The measured strain reduction was approximately 28% and was equivalent to the reduction in the nett section stress.

8.5. Remarks

This section has presented a repair methodology that can be used as a first approximation for field repairs to damaged composite structures. It has also been shown that an externally bonded doubler was able to repair impact damage, even for thick structural components. The use of externally bonded patches has the advantage of being quick and easy to apply. The F/A-18 horizontal stabilator repair also indicated that extensive removal of damaged material, excluding penetration clean up, can be avoided thereby making the repair process particularly simple.

9. CONCLUSIONS AND RECOMMENDATIONS

This report has attempted to clarify the fundamental mechanisms responsible for the degradation, in both static strength and fatigue performance, due to low velocity impact damage. It has been shown that for the development of a damage tolerant philosophy a consistent test and analysis methodology is required for measuring and computing the critical energy release rates. For Modes II and III this methodology should allow for both in-elastic effects and for strain rate effects.

It has also been shown that for delamination damage in:

(a) composite laminates,

(b) at step lap joints, or

(c) at mechanically fastened composite joints,

a stage is reached after which a significant increase in the size of the damage does not significantly reduce the residual strength. This significantly simplifies the methodology for estimating critical damage size. It has also been shown that, in fatigue, there is a well defined endurance limit and that small changes in the cyclic stress amplitude can produce very large changes in fatigue life. In contrast to the situation for cracks in metallic structural components, load bi-axiality has a marked effect on residual strength. This means that for service aircraft the residual strength and the strength after repair cannot be estimated using either uni-axial test specimens or via simplistic one dimensional analysis. This conclusion needs to be validated experimentally.

A simple repair design methodology, that can be used as a first approximation for field repairs to damaged composite structures, has also been presented and it has been shown that an externally bonded doubler was able to repair impact damage, even for thick structural components. The F/A-18 Horizontal Stabilator repair indicated that extensive removal of damaged material, excluding penetration clean up, can be avoided thereby making the repair process particularly simple.

REFERENCES

1. Baker, A.A., Jones, R. & Callinan, R.J., Damage tolerance of graphite/epoxy composites. *Composite Structures*, **4** (1985) pp. 15-44.
2. Badaliance, R. & Dill, H.D., Damage mechanism and life prediction of graphite-epoxy composites. *Damage in Composite Materials*, ASTM STP 775, 1982, pp. 229-42.
3. Schutz, D., Gerharz, J.J. & Alschweig, E., Fatigue properties of unnotched, notched and jointed specimens of a graphite-epoxy composite. *Fatigue of Fibrous Composite Materials*, ASTM STP 723, 1981, pp. 31-47.
4. Prakash, R., Significance of defects in the fatigue failure of carbon fibre reinforced plastics. *Fibre Science and Technology*, **14** (1981) pp. 171-81.
5. Talreja, R., A conceptual framework for the interpretation of fatigue damage mechanisms in composite materials. *J. Composites Technology and Research*, **7** (1985) pp. 25-9.
6. Harris, B., Fatigue and accumulation of damage in reinforced plastics. *Composites*, **8** (Oct.) (1977) pp. 214-20.
7. Ramkumar, R.L., Compression fatigue behaviour of composites in the presence of delaminations. *Damage in Composite Materials*, ASTM STP 775, 1982, pp. 184-210.
8. O'Brien, T.K., Mixed-mode strain-energy-release rate effects on edge delamination of composites. *Effects of Defects in Composite Materials*, ASTM STP 836, 1984, pp. 125-42.
9. Jones, R., Broughton, W., Mousley, R.F., & Potter, R.T., Compression failures of damaged graphite epoxy laminates. *Composite Structures*, 3 (1985) pp. 167-86.
10. Ramkumar, R.L., Effect of low-velocity impact damage on the fatigue behaviour of graphite-epoxy laminates. *Long-Term Behaviour of Composites*, ASTM STP 813, 1983, pp. 116-35.
11. Rosenfeld, M.S. & Gause, L.W., Compression fatigue behaviour of graphite-epoxy in the presence of stress raisers. *Fatigue of Fibrous Composite Materials*, ASTM STP 723, 1981, pp. 174-96.
12. Adsit, N.R. & Waszczak, J.P., Effect of near visual damage on the properties of graphite-epoxy. *Composite Materials: Testing and Design, Fifth Conference*, ASTM STP 647, 1979, pp. 101-17.
13. Starnes, J.H., Jr, Rodes, M.D. & Williams, J.G., Effect of impact damage and holes on the compressive strength of a graphite/epoxy laminate, *Nondestructive Evaluation and Flaw Criticality for Composite Materials*, ASTM STP 696, 1979, pp. 145-71.

14. Williams, J.G., O'Brien, T.K. & Chapmen, A.J. III, Comparison of toughened composite laminates using NASA standard damage tolerance tests, *ACEE Conference on Composite STructures Technology, Seattle, WA*, 13-15 Aug., 1984.

15. Cardon, H.D., Impact dynamics research on composite transport structures, *ACEE Conference on Composite Structures Technology, Seattle, WA*, 13-15 Aug., 1984.

16. Bradley, W.L. & Cohen, R.N., Matrix deformation and fracture in graphite-reinforced epoxies. *Delamination and Debonding of Materials*, ASTM STP 876, 1985, pp. 389-410.

17. Chai, H., The characterization of Mode I delamination failure in non-woven, multidirectional laminates. *Composites*, **15** (4) (1984) pp. 277-90.

18. Wilkins, D.J., Eisenmann, J.R., Camin, R.A., Margolis, W.S. & Benson, R.A., Characterizing delamination growth in graphite-epoxy. *Damage in Composite Materials*, ASTM STP 775,1982, pp. 168-83.

19. Ramkumar, R.L. & Whitcomb, J.D., Characterization of mode I and mixed-mode delamination growth in T300/5208 graphite epoxy. *Delamination and Debonding of Materials*, ASTM STP 876, 1985, pp. 315-35.

20. Russell, A.J. & Street, K.N., Factors affecting the inter-laminar fracture energy of graphite/epoxy laminates. *Progress in Science and Engineering of Composites, ICCM-IV*, Tokyo, Japan Society of Composite Materials, 1982.

21. Aliyu, A.A. & Daniel, I.M., Effects of strain rate on delamination fracture toughness of graphite/epoxy. *Delamination and Debonding of Materials*, ASTM STP 876,1985, pp. 336-48.

22. Whitney, J.M. & Browning, C.E., Materials characterization for matrix-dominated failure modes. *Effects of Defects in Composite Materials*, ASTM STP 836, 1984, pp. 104-24.

23. O'Brien, T.K., Analysis of local delaminations and their influence on composite laminate behaviour. *Delamination and Debonding of Materials*. ASTM STP 876, 1985, pp. 282-97.

24. O'Brien, T.K., Characterization of delamination onset and growth in a composite laminate. *Damage in Composite Materials*, ASTM STP 775, 1982, pp. 140-67.

25. Whitney, J.M. & Knight, M., A modified free-edge delaaamination specimen. *Delamination and Debonding of Materials*, ASTM STP 876, 1985, pp. 298-314.

26. Donaldson, S.L., Fracture toughness testing of graphite/epoxy and graphite/PEEK composites. *Composites*, **16** (2) (1985) pp. 103-12.

27. Russell, A.J. & Street, K.N., The effect of matrix toughness on delamination: static and fatigue fracture under mode II shear loading of graphite fibre composites. Paper presented at *NASA/ASTM Symposium on Toughened Composites*, Houston, 13-15 March, 1985.

28. Byers, B.A., Behaviour of damaged graphite epoxy laminates under compression loading, *NASA-CR-159293*, Final Report, Dec. 1979, 1980.

29. Jurf, R.A. & Pipes, R.B., Interlaminar fracture of composite materials. *Composite Materials*, **16** (1982) pp. 386.

30. Nicholls, D.J. & Gallagher, J.P., Determination of G_{Ic} in angle ply composites using a cantilever beam test method. *J. Reinforced Plastics and Composites*, **2** (1983) pp. 2.

31. Wang, A.S.D., Kishore, N.N. & Fong, W.W., On mixed-mode fracture in off-axis unidirectional graphite/epoxy composites. *Process in Science and Engineering of Composites*, ICCM-IV, Tokyo, Japan Society for Composite Materials, 1982.

32. Chatterjee, S.N., Pipes, R.B. & Blake, R.A. Jr, Criticality of disbonds in laminated composites. *Effects of Defects in Composites Materials*, ASTM STP 836, 1984, pp. 161-74.

33. Demuts, E. & Horton, R.E., Damage tolerant composite design development. In *Composite Structure-3*, ed. Marshall, I.H., Elsevier Applied Science Publishers Ltd, London, 1985.

34. Potter, R.T., The interaction of impact damage and tapered-thickness sections in CFRP. *Composite Structures*, **3** (1985) pp. 319-39.

35. Ryder, R.J., Lauraitis, K.M. & Pettit, D.E., Advanced residual strength degradation rate modelling for advanced composite structures. *AFWAL-TR-79-3095*, Vol. II, Tasks II and III, July 1981.

36. Dorey, G., Structural life predictions for fibre reinforced composite materials. *ONR Workshop on Damage Tolerance of Fibre Reinforced Composite Materials*, Glasgow, UK, 12 Sept., 1985.

37. O'Brien, T.K., Interlaminar fracture of composites. *J. Aeronautical Society of India*, **37** (1985) pp. 61-9.

38. Black, N.F. & Stinchcomb, W.W., Compression fatigue damage in thick, notched graphite-epoxy laaminates. *Long-term Behaviour of Composites*, ASTM STP 813, 1983, pp. 95-115.

39. Rosenfeld, M.S. & Huang, S.L., Fatigue characteristics of graph-epoxy laminates under compression loading. *J. Aircraft*, **15** (1978) pp. 264-8.

40. Ratwani, M.M. & Kan, H.P., Compression fatigue analysis of fibre composites. *NADC-78047-69*, Sept., 1979.

41. Stellbrink, K.K. & Aoki, R.M., Effect of defect on the behaviour of composites. *Progress in Science and Engineering of Composites*, ICCM-IV, Tokyo (1982).

42. Demuts, E., Whitehead, R.S. & Deo, R.B., Assessment of damage tolerance in composites. *Composites Structures*, **4** (1985) pp. 45-58.

43. Walter, R.W., Johnson, R.W., June, R.R. & McCarty, J.E., Designing for integrity in long-term composite aircraft structures. *Fatigue of Filamentary Composite Materials*, ASTM STP 636, 1977, pp. 228-47.

44. Stellbrink, K.K., On the behaviour of impact damage CFRP laminates. *Fibre Science and Technology*, **18** (1983) pp. 81-94.

45. Hart-Smith, L.J., The design of repairable advanced composite structures. *Douglas Paper 7550*, 14-17 Oct., 1985.

46. Byers, B.A., Behaviour of damaged graphite epoxy laminates under compression loading. *NASA-CR-159293*, Final Report, Jan. 1978-Dec. 1979, Aug. 1980.

47. Chatterjee, S.N., Pipes, R.B. & Blake, R.A., Jr. Criticality of Disbonds in Laminated Composites. ASTM STP 836, 1984, pp. 161-74.

48. Mohlin, T., Blom, A.F., Carlsson, L.F. & Gustavsson, A.I., Delamination Growth in a Notched Graphite/Epoxy Laminate under Compression Fatigue Loading. ASTM STP 876, 1985, pp. 168-88.

49. O'Brien, T.K., Characterization of Delamination Growth in a Composite Laminate. ASTM STP 775, 1982, pp. 140-67.

50. Ramkumar, R.L. & Whitcomb, J.D., Characterization of Mode I and Mixed-Mode Delamination Growth in T300/5208 Graphite/ Epoxy. ASTM STP 876, 1985, pp. 315-35.

51. Wang, A.S.D., Slomania, M. & Bucinell, R.B., Delamination Crack Growth in Composite Laminates. ASTM STP 876, 1985, pp. 167-235.

52. Russell, A.J. & Street, K.N., The effect of matrix toughness on delamination: static and fatigue fracture under NASA/ASTM. *Symposium on Toughened Composites, Houston,* 13-15 March, 1985.

53. Whitcomb, J.D., Strain Energy Release Rate Analysis of Cyclic Delamination Growth in Compressively Loaded Laminates. ASTM STP 836, 1984, pp. 175-93.

54. Atluri, S.N., *Computational Methods in the Mechanics of Fracture*, North Holland, Amsterdam, 1986.

55. Jones, R., Tay, T.E. & Williams, J.F., Thermo-mechanical behaviour of composites. In: *Composite Material Response: Constitutive Relations and Damage Mechanicsm* (Ed. G.C. Sih *et al.*), Elsevier Applied Science Publishers, 1988, Chapter 3.

56. Atluri, S.N., Nakaguki, M., Nishioka, T. & Kuang, Z.B., Crack tip parameters and temperature rise in dynamic crack propagation. *Engineering Fracture Mechanics*, **23** (1) (1986) pp. 167-82.

57. Timoshenko, S. & Gere, J.M., *Theory of Elastic Stability*, 2nd Edition, McGraw-Hill, New York, (1961).

58. Evans, A.G. & Hutchinson, J.W., On the mechanics of delamination and spalling in compressed films. *Int. J. Solids Struc.* **20** (1984) pp. 455-466.

59. Partridge, C., Williams, J.F., Jones, R. & Waechter, R.T., Analysis of the delamination behaviour in a compressed circular laminate. *Int. Report No. SM/2/87,* Dept. of Mechanical and Manufacturing Engineering, University of Melbourne, Victoria, Australia (1987).

60. Jones, R., Callinan, R., Teh, K.K. and Brown, K.C., Analysis of multilayer laminates using three-dimensional super elements. *Int. J. Numer. Methods Eng.*, **18** (1984) pp. 583-7.

61. Hansen, J.S., Bowers, C.P., Mabson, G.E., Papathanassis, N., Tennyson, R.C., Wharram, G.E. and Elliott, W.G., Investigation of static failure and fatigue life of unflawed and flawed graphite/epoxy laminates: analysis and experiments. Part 2: finite element models. Defence Research Establishment Pacific, *DREP97708-2-2721*, December, 1984.

62. Bascom, W.D., Bitner, J.L., Moulton, R.J. and Siebert, A.R., The interlaminar fracture of organic-matrix, wover reinforcement composites. *Composites*, January (1980) pp. 9-18.

63. Curtis, P.T., CRAG test methods for the measurement of the engineering properties of fibre reinforced plastics. *RAE TR 84102*, October, 1984.

64. Tay T.E., Williams J.F., & Jones R., Application of the T* integral and S criteria in finite element analysis of impact damaged fastener holes in graphite/epoxy laminates under compression. *Composite Structures* **7** (1987) pp 233-253.

65. Chen, J.K. & Sun, C.T., Nonlinear analysis of interlaminar stress in graphite/epoxy laminates with and without delamination cracks. Paper presented at *6th International Conference on Composite Materials*, July 1987, London, UK.

66. Wong, A.K. & Jones, R., A numerical study of two integral type elasto-plastic fracture parameters under cyclic loading. *Engng Frac. Mech* **26** (5) (1987) pp 741-1752.

67. Tay, T.E. , Paul J. & Jones R., Effects of plasticity on several fracture parameters for impact damage and related problems. *Composite Structures* **18** (2) (1991) pp. 109-124.

68. Paul, J. & Jones, R., Repair of impact damaged composites. *Journal of Engineering Fracture Mechanics* **41** (1) (1992) pp. 127-141.

69. Jones, R., Paul, J., Tay, T.E., and Williams, J.F., Assessment of the effect of impact damage in composites: some problems and answers. *Theoretical and Applied Fracture Mechanics* **9** (1988) pp. 83-95.

70. Paul, J., Evaluation of a damaged F/A-18 horizontal stabilator. *Aircraft Structures Technical Memorandum 503*, Aeronautical Research Laboratory, Melbourne, Australia, February, 1989.

71. Jones, R., Heller, M., Sparrow, J.G. and Ryall, T.G., A new approach to structural optimisation. *Composites Structures* **16** (1990) pp. 1-32.

72. Paul, J. and Bridgford, N., Stress analysis of a damaged F/A-18 horizontal stabilator. *Aircraft Structures Technical Memorandum 510*, Aeronautical Research Laboratory, Melbourne, Australia, May, 1989.

73. Chiu, W.K., Rees, D., Chalkley, P. and Jones, R., Designing for damage tolerant repairs. *Aircraft Structures Report 450*, Aeonautical Research Laboratory, Melbourne, August 1992.

74. Paul, J., Galea, S.C. and Jones, R., Residual strength of composites with multiple impact damage. *ARL Research Report (in press).*

75. Partridge, C., Waechter, R.T., Williams, J.F. and Jones, R., Understanding delamination behaviour in a circular laminate. *Theoretical and Applied Fracture Mechanics* **13** (2) (1990) pp. 99-104.

76. van Blaricum, T.J., Bates, P. and Jones, R., An experimental investigation into the effect of impact damage on the compressive strength of step lap joints. *Journal of Engineering Fracture Mechanics* **32** (5) (1989) pp. 667-674.

77. Chow, C.L. & Woo, C.W., On flaw size and distribution in lap joints. *Theoretical and Applied Fracture Mechanics* **4** (1) (1985) pp. 75-82.

Table 1a: Comparison of experimental values of G_{Ic} from the literature

Material	*Reference*	*Test method*	G_{Ic} (J/m^2)
T300/5208	Wilkins *et al.*[18]	DCB	87.6
T300/5208	Ramkumar & Whitcomb[19]	DCB	102.6
T300/5208	Chai[17]	DCB	86±8
T300/5208	O'Brien[23]	EDT	137
T300/5208	Byers[28]	Modified width-tapered DCB	160-241
GY70/5208	Russel & Street[20]	DCB	83
AS1/3501-6	Russel & Street[20,27]	DCB	110
AS1/3501-6	Jurf & Pipes[29]	Modified Arcan Test	79
AS4/3501-6	Aliyu & Daniel[21]	DCB	198-232
AS1/3502	Bradley & Cohen[16]	DCB	155
AS1/3502	Whitney & Browning[22]	DCB	140
AS1/3502	Nicholls & Gallagher[30]	DCB	105-175
AS1/3502	Bradley & Cohen[16]	CT (Compact Tension)	225
AS1/3502	Whitney & Browning[22]	90° CN	154
AS1/3502	Whitney & Browning[22]	EDT	267
AS4/3502	Bradley & Cohen[16]	DCB	225#
AS4/3502	Bradley & Cohen[16]	CT	120
AS4/3502	Whitney & Knight[25]	EDT 50.8 mm wide specimen	103
AS4/3502	Whitney & Knight[25]	EDT 25.4 mm wide specimen	238
AS4/3502	Whitney & Knight[25]	EDT modified with inserts	81-96
AS4/3502	Whitney & Knight[25]	DCB	158
T300/1034C	Donaldson[26]	90° CN	77.9
T300/934	O'Brien[24]	EDT	216
T300/934	Wang *et al.*[31]	DEN (Double Edge Notched)	157

extensive fibre bridging observed.

Table 1b: Description of analysis and experiment for determining G_{Ic}

Reference	*Test method*	*Description*
Wilkins *et al.*[18]	DCB	Compliance method of test procedure employed, i.e. $G = P^2(dC/da)/2W$. Load-displacement curve monitored for static loading. Relationship between compliance and crack length was obtained, $C = 2a^3/3E1 = A_1a^3$. Also, the relationship, $P_c = (G_cWEI)^{1/2}/a = A_2/a$ was obtained. The value of G_c can then be calculated. Both experimental curves of C vs a and P_c vs a were obtained via a least-squares-fit routine to obtain A_1 and A_2.
Ramkumar & Whitcomb[19]	DCB	Similar data analysis as in Wilkins *et al.*[18].
Russell & Street[20]	DCB	Similar data analysis as in Wilkins *et al.*[18].
Bradley & Cohen[16]	DCB	Analysis based on linear beam theory. $G_I = 8P_s^2/L_c^2/WEI$, where P_s is the applied load, L_c is the length of the split laminate. The analysis was essentially similar to Wilkins *et al.*[18].
Aliyu & Daniel[21]	DCB	Beam analysis method used. The analysis was extended to include transverse shear deformation and kinetic energy effects on the energy release rate. A semi-empirical method based on the assumption of partial elastic foundation support beyond the crack tip was proposed. Effect of crack velocity on energy release rate studied. G_{Ic} found to increase with crack velocity.
Whitney & Browning[22]	DCB	G_{Ic} obtained through the relationship $G_{Ic} = 1/26\Delta c(P_1\delta_2 - P_2\delta_1)$, where P_1 and P_2 are the loads before and after crack extension, δ_1 and δ_2 the deflections before and after crack extension, and Δc the increment in crack extension. The analysis was based on area between the loading and unloading curves.
Chai[17]	DCB	Semi-empirical method of analysis used. An empirical relationship between compliance C and crack length l, $C = al^n$, where a and n are constants, was used to obtain: $$G_I = \frac{n}{2b}\frac{P\delta}{l}$$
Jurf & Pipes[29]	Modified Arcan test on Single Edge Notch	The aluminium fixtures enabled mixed-mode loading of the specimen by varying the angle of loading α. For pure Mode I loading, $\alpha = 90°$ and the applied stress normal to the crack plan was $\sigma = P/A$, where P is the applied load and A is the area of specimen on which the load is applied. There was some scatter in the values of K_{Ic} obtained. G_{Ic} was obtained from K_{Ic}.

Table 1b: Cont'd

Reference	*Test method*	*Description*
Byers[28]	DCB	Width-tapered specimens for comparison of interlaminar fracture toughness of composites with different resin systems. However, the aluminum tabs were actually half-inch-thick plates adhesively bonded to the entire top and bottom surfaces of the laminated specimen. The values of G_{Ic} obtained were much higher than those obtained by others using normal DCB specimens, probably due to increased stiffness introduced by the aluminium plates. The expression $G_{Ic} = 12P^2/(Eh)(a/b)^2$ was used, where P is the crack initiation load and (a/b) is the specimen taper ratio.
Donaldson[26]	90° CN	G_{Ic} was obtained through calculation of $K_{Ic} = \sigma_{NC}\sqrt{\pi a}$, where a is the half crack length, and σ_{NC} is the far-field stress normal to the crack. G_I was associated with K_I via an equation containing the orthotropic material properties.
Whitney & Browning[22]	90° CN	G_{Ic} obtained through calculation of $K_{Ic} = \sigma_n^{\infty}\sqrt{\pi(a+a_0)}$, where a_0 is an inherent flaw determined from the average stress criterion, σ_n^{∞} is the notch strength of plate of infinite extent. σ_n^{∞} was obtained from σ_w, the strength of a tensile coupon with finite width, via an isotropic width correction relationship. G_{Ic} was obtained from K_{Ic}. G_{Ic} obtained was higher than values obtained through 0° DCB tests.
Wang *et al.*[31]	DEN	G_I available at notch-tip calculated by a two-dimensional plane-stress finite element routine.
Bradley & Cohen[16]	CT	Displacement-load relationship monitored. Tests conducted in displacement control to allow stable crack growth. Standard linear fracture mechanics relationship $G_I = (P^2/2B)(\partial C/\partial a)$ used.
O'Brien[23,24]	EDT	Laminated plate theory and simple rule of mixture for stiffness loss due to delaminations were used to derive $G_c = \frac{\varepsilon_c^2 T}{2}(E_{LAM} - E^*)$ where E_{LAM} is the stiffness of plate calculated from laminated plate theory, E^* is the stiffness of partially delaminated laminate, ε_c is the critical strain at the onset of delamination, and T is the laminate thickness.

Table 1b: Cont'd

Reference	*Test method*	*Description*
Whitney & Knight[25]	Modified EDT	Specimens had free-edge starter cracks of length a embedded in the centre plane of specimens. Classical laminated plate theory invoked to obtain $G_{Ic} = h\varepsilon_c^2(E_x - E^*)$, where h is the half thickness of laminate, ε_c is the critical strain, and E_x and E^* are modified inplane stiffness terms. E^* here is not the same as O'Brien's E^*. Values of G_{Ic} obtained slightly lower than those from unmodified EDTs.
Whitney & Browning[22]	EDT	Laminated plate theory used to derive $G_{Ic} = h\varepsilon_c^2(1 - E_1^*/E_1)\overline{E}_1$ where h is half laminated thickness, ε_c is the critical strain at delamination, E_1 is the laminate modulus in the load direction, E_1^* is an effective laminate modulus for delaminated composite, and $\overline{E}_1$ is the experimentally determined value of E_1. Both E_1 and E_1^* were calculated from laminated plate theory. If $\overline{E}_1 = E_1$, then the expression for G_{Ic} would be the same as O'Brien's expression.

Table 2: Comparison of experimental values of G_{IIc} from the literature

Reference	*Description of test method and analysis*	*Material*	G_{IIc} (J/m^2)
Wilkins *et al.*[18]	CLS (Cracked Lap Shear) specimens: Relative proportions of G_I and G_{II} obtained through finite element analysis. Proportion of Mode II, G found to be approx. 75% of total energy release rate.	T330/5208	154
Ramkumar & Whitcombe[19]	CLS specimens. The embedded delamination did not always propagate along the midplane, but crossed over to the adjacent interface. A simple strength-of-materials analysis of CLS specimen to account for the change in stiffness due to the crossover was used to compute the change in compliance with crack length, dC/da. A geometrically non-linear finite element analysis was performed to determine the relative proportions of G_I and G_{II} at the critical load. G_c was obtained experimentally. Values of G_I, G_{II} and G_{Ic} were substituted into three failure criteria and G_{IIc} obtained: (a) $G_I/G_{Ic}+G_{II}/G_{IIc}=1$, (b) $(G_I/G_{Ic})^2+(G_{II}/G_{IIc})^2=1$, (c) $(G_I/G_{Ic})^2+(G_{II}/G_{IIc})^2+(G_I/G_{Ic})+(G_{II}/G_{IIc})=1$.	T300/5208	876,criterion(a) 456,criterion(b) 643,criterion(c)
Russell & Street[20,27]	ENF (End Notched Flexural) specimens. Specimens were subjected to three point flexural loading. The Teflon started notch tip was placed midway between two loading pins. Beam theory analysis was used to obtain dC/da to be substituted into the expression for G_{IIc}, yielding $G_{IIc}=9a^2P^2C_b/2b(2L^3+3a^3)$, where C_b is the compliance due to bending.	AS1/3501-6 HMS/3501-5 AS4/2220-3	452±6 152±11 750±25
Chatterjee *et al.*[32]	Three Point Bend Test specimens. Implanted defects in the form of two-ply Teflon delaminations were located in the region of compressive flexural stress. A computer code was used to solve the problem of disbonds between two piles. Some of the specimens were fatigued to produce sharp crackfronts.	AS1/3501-6	1042±214 Blunt crack tips 950±175 Sharp crack tips
Donaldson[26]	Modified Three Rail Shear Test. This was not a delamination test, but an in-plane crack was cut into an unidirectional laminate parallel to the fibre direction. Earlier finite element analysis by Lakshminarayana showed a uniform state of in-plane shear stress throughout the central region of the specimen. This shear stress was computed via $\tau_c = P_c/2tl$, where P_c is the critical applied load, t and l are the specimen thickness and length respectively. The stress intensity factor $K_{IIc} = \tau_c\sqrt{\pi a}$ where a is the half crack length, was computed and the value of G_{IIc} thus calculated.	T300-1034C	506

Table 2: Cont'd

Reference	*Description of test method and analysis*	*Material*	G_{IIc} (J/m^2)
Jurf & Pipes[29]	Modified Arcan Test on Single Edge Notch specimens. The fixtures enabled mixed-mode loading of the specimen by varying the angle of loading, α. The stresses applied to the specimen were simply $\sigma = (P\sin\alpha)/A$ for the normal stress, and $\tau = (P\cos\alpha)/A$ for the shear stress, where A was the area of specimen through which the load was transmitted. The specimens were 91 ply thick, with teflon inserts, and where adhesively bonded to the aluminium Arcan fixtures. For Mode II loading, α = 0°. Some specimens failed at the metal-composite adhesive bond. K_{IIc} was obtained and related to G_{IIc}.	AS1/3501-6	670

Table 3: Summary of experimental data on *S-N* curves derived from the literature

Reference	*Maximum compressive strain range*	*Maximum compressive stress range*	*Range of cycles to failure*	*Comments*
Rosenfeld & Gause[11]	2400-3000με (i.e. $\Delta\varepsilon$ = 600με)		2×10^3 - 2×10^6	Laminated plate specimens; AS/3501-6; 48 ply; Delamination area 12.9 cm^2; 16.4 J impact; $R = -\infty$
Demuts *et al.*[42]	Strain fixed at 3000με		10^4 - 10^6	Multirib specimens; AS6/2220-3; 136 J impact; R = 10.
Demuts & Horton[33]	S = 0.6-0.7[#]		5×10^4 - 10^6	3-stiffener panel; AS6/2220-3; 136 J impact; R = 10.
Walter *et al.*[43]	S = 0.28-0.30		10^4 - 10^6	Laminated plate specimens; T300/5208; 6.2 J impact; R = -1.0.
Stellbrink & Aoki[41] Stellbrink[44]		200-250 MPa (i.e. $\Delta\sigma$ = 50 MPa)	0 - 10^5	Laminated plate specimens; T300/CODE69; 18 ply; Impacted with ball of mass 255 g and radius of 5 mm at velocity of 6.15 m/s; R = -1.0.
Potter[34]		Stress level fixed at 206 MPa	622 - 8242[+]	Tapered-thickness specimens; XAS/914; 32 ply - 24 ply; 5.0 J impact; R = 10.
Ryder *et al.*[35]		Stress level fixed at 241 MPa	2×10^4 - 10^6	24 ply damaged hole specimens; R = -1.0.
		Stress level fixed at 152 MPa	2×10^4 - 5×10^5	32 ply damaged hole specimens; R = -1.0.

[#] S is the ratio of the average peak fatigue load to damaged residual static strength.
[+] Test terminated before specimen failed.

Table 4: Values of the exponent '*n*' in the growth law $(da/dN)=c(G)^n$ as predicted by various studies for Mode I, Mode II, and Mixed Mode cases

Reference	*Exponent 'n'*	
	Mode I	*Mixed-Mode or Mode II*
Wilkins *et al.*[18]		
Wang *et al.*[51]	20 - 30	7-8 (Mixed-Mode)
Ramkumar & Whitcomb[50]	8 - 10	6 (Mixed-Mode)
O'Brien[49]	3 - 3.5	-
Chatterjee *et al.*[47]	-	2.4 (Mode II)
Whitcomb[53]	15 - 20	-

Table 5: Values of the exponent '*n*' in the growth law $(da/dN)=c(\Delta G_{II})^n$ as developed by Russell & Street[52] in the order of increasing toughness

Exponent 'n'	*Material*	
5.79	AS1/3501-6	First generation high temperature graphite-epoxy
5.71	AS4/2220-3	Second generation high temperature graphite-epoxy
4.52	C6000/F155	An intermediate temperature rubber toughened graphite-epoxy
3.88	AS4/APC2	High temperature graphite-thermoplastic composite

Table 6: Properties of T300/5208

	E_{11} (GPa)	E_{22} (GPa)	υ_{12}	G_{12} (GPa)	G_{13} (GPa)	G_{23} (GPa)
Case 1 - Equal shear moduli	141.33	9 45	0.31	5.18	5.18	5.18
Case 2 - Unequal shear moduli	141.33	9 45	0.31	5.18	5.18	3.63

TABLE 7: Properties of matrix material

E_m (GPa)	υ_m
3.50	0.3

Table 8

Maximum value of the ratio of plastic to elastic fracture parameter
$\frac{T^*_{plastic}}{T^*_{elastic}} = 1.157$

Table 9: Summary of T^* (max value) and its angular location θ_T

Case	T^*	θ_T	*Predicted* T^*
1UN	0.0907	30°	--
2UN	0.0901	30°	--
3UN	0.0687	45°	--
1UR	0.0471	45°	0.0403
2UR	0.0470	45°	0.0400
3UR	0.0376	45°	0.0305
1BN	0.1390	30°	--
2BN	0.1390	30°	--
3BN	0.0992	30°	--
1BR	0.0669	30°	0.0618
2BR	0.0669	30°	0.0618
3BR	0.0514	30°	0.0441

Case Description: 1 - Open hole, 2 - Interference Fit Fastener, 3 - Bonded Insert,
U - Uniaxial Load, B - Biaxial Load, N - No Repair, R - Repaired.

Table 10: Results of static compression tests: Single impact case

Specimen number	*Impactor diameter* (mm)	*Absorbed energy* (J)	*Damaged area* (mm^2)	*Unrepaired (U) Required (R)*	*Failure load* (kN)	*Failure strain* (με)	*Predicted strain* (με)
1	19.8	7.59	453	U	-191	-4503	--
2	19.8	7.55	453	U	-214	-4680	--
3	19.8	7.96	453	U	-213	-4826	--
4	19.8	5.60	479	R	-238	-4993*	-6164
5	19.8	8.21	428	R	-238	-4993*	-6164
6	19.8	7.84	448	R	-289	-6699	-6164
7	19.8	7.88	458	R	-289	-6699	-6164
8	30.0	7.46	733	U	-168	-4097	--
9	30.0	6.93	718	U	-192	-4375	--
10	30.0	7.88	665	U	-173	-4305	--
11	30.0	7.54	761	U	-196	-4350	--
12	30.0	7.74	761	U	-197	-4274	--
13	30.0	7.67	761	U	-178	-4025	--
14	30.0	7.66	800	R	-233	-5293	-5594
15	30.0	7.35	800	R	-233	-5293	-5594
16	30.0	7.45	739	R	-227	-5554	-5594
17	30.0	7.64	704	R	-227	-5554	-5594
18	39.7	6.25	1252	U	-178	-4061	--
19	39.7	5.76	1252	U	-204	-4445	--
20	39.7	5.87	1252	U	-181	-4090	--
21	39.7	7.83	1385	R	-238	-5337	-5542
22	39.7	7.58	1212	R	-238	-5337	-5542
23	39.7	7.70	1290	R	-222	-5099	-5542
24	39.7	7.59	1120	R	-333	-5099	-5542

* Specimens exhibited extensive bending prior to failure (anti-buckling rig was distorted)

Table 11: Strain gauge results for the damaged and undamaged skins on the CREDP horizontal stabilator: Compression case (all measurements in με)

RBM (kNm)		0	-9	-18	-25	-31	-25	-18	-9	0
Torque (kNm)		0	-6	-13	-18	-22	-18	-13	-6	0
Gauge D1	+45	-1	-131	-258	-361	-453	-369	-269	-144	-1
Gauge D1	0	-1	-263	-516	-717	-899	-732	-531	-283	-1
Gauge D1	-45	0	-49	-95	-132	-164	-132	-96	-51	-1
Gauge D2	+45	-1	-64	-125	-175	-219	-176	-127	69	-1
Gauge D2	0	0	-119	-232	-321	-400	-327	-240	-129	-1
Gauge D2	-45	-1	-12	-24	-32	-39	-33	-30	-17	-1
Gauge D3	+45	0	-182	-356	-496	-622	-505	-366	-194	-1
Gauge D3	0	-	423	-827	-1151	-1437	-1156	-831	-434	-2
Gauge D3	-45	0	-95	-186	-259	-325	-262	-191	-101	-2
Gauge D4	+45	-1	-126	-246	-344	-431	-351	-256	-138	-1
Gauge D4	0	-1	-261	-508	-705	-878	-717	-522	-281	-1
Gauge D4	-45	-1	-25	-47	-63	-78	-645	-48	-27	-1
Gauge U1	+45	0	119	232	322	401	328	238	127	-1
Gauge U1	0	-1	260	507	705	877	714	518	275	-1
Gauge U1	-45	0	60	119	165	204	164	118	60	-1
Gauge U2	+45	-1	113	219	304	376	308	224	119	-1
Gauge U2	0	-1	161	316	440	550	446	320	168	-1
Gauge U2	-45	-1	-16	-27	-36	-42	-39	-37	-24	-1
Gauge U3	+45	-1	171	333	463	573	467	339	180	-1
Gauge U3	0	-1	405	790	1097	1357	1107	804	429	-1
Gauge U3	-45	-1	112	218	302	373	304	220	117	-1
Gauge U4	+45	-1	93	182	252	311	252	181	95	-1
Gauge U4	0	-1	257	502	702	872	708	513	272	0
Gauge U4	-45	0	-3	-6	-8	-10	-8	-6	-3	0
U		1	370	734	1038	1285	1067	788	438	0
D		0	-363	-719	-1016	-1260	-1041	-754	-403	0

Table 12: Laminate properties for the horizontal stabilator skin and repair doubler

	E_{XX} (GPa)	E_{YY} (GPa)	G_{XY} (GPa)	ν_{XY}	ν_{YX}
Skin	66.7	32.5	14.5	0.389	0.190
Repair	57.4	32.9	17.2	0.443	0.253

Table 13: Summary of strain results from finite element analysis at DLBM

Strain gauge number	*Unrepaired* με	*Repaired* με	*% Reduction*
1	4,953	3,557	28
2	4,621	3,399	26
3	5,210	3,658	30
4	4,863	3,522	28
LVDT	5,284	3,664	31

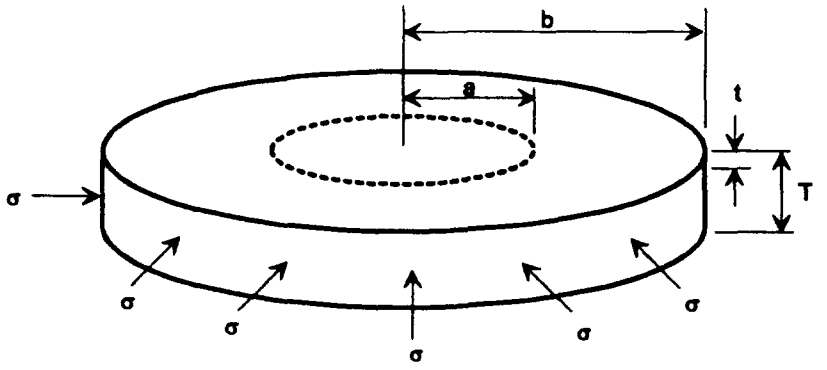

Figure 1. Plane view of the delamination.

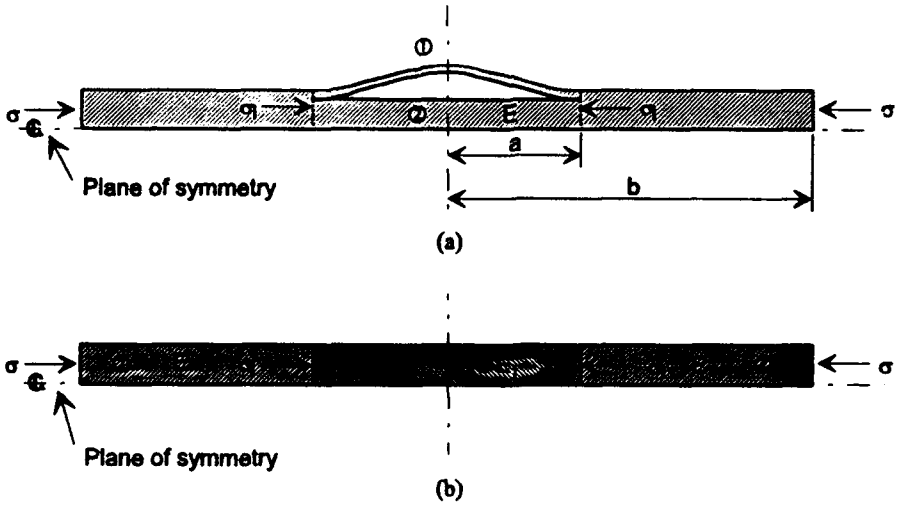

Figure 2. Cross-sectional view of the delamination. (a) Specimen A, (b) Specimen B.

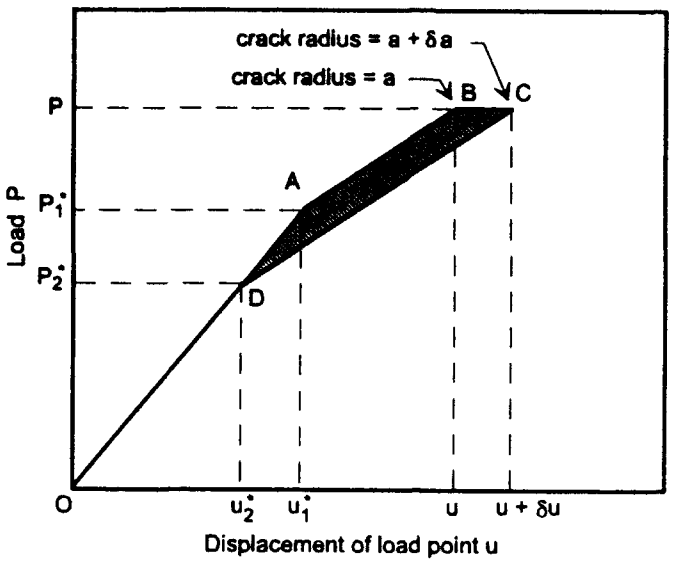

Figure 3. Typical load/deflection curve.

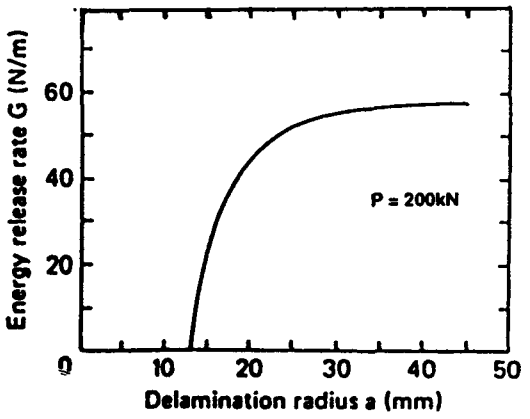

Figure 4. Variation of G with radius.

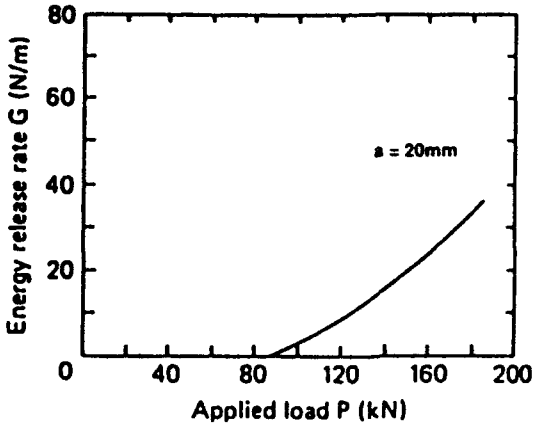

Figure 5. Variation of G with load.

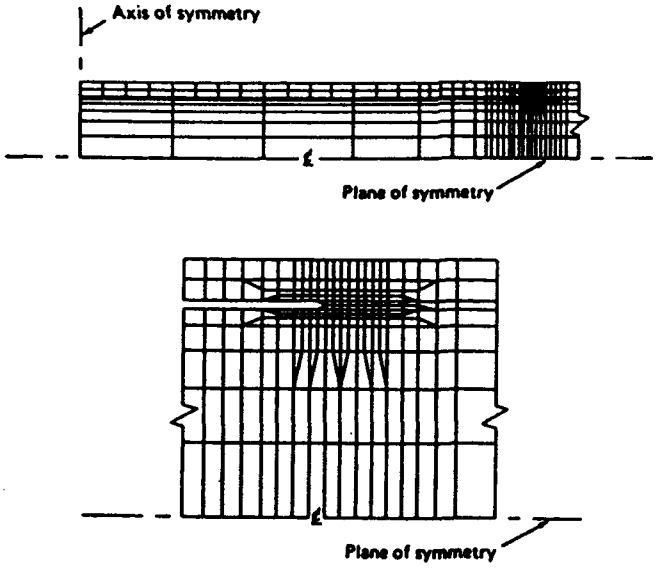

Figure 6. Mesh geometry.

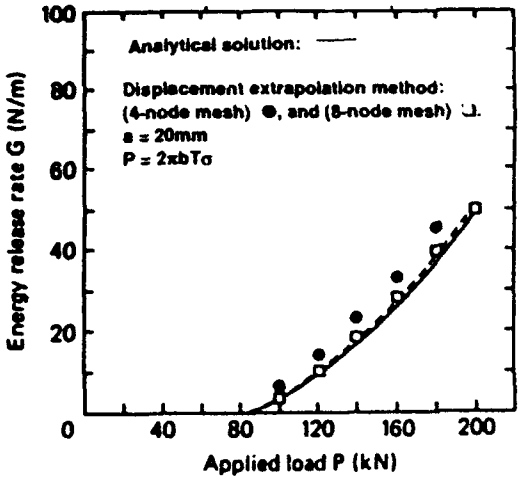

Figure 7. Plot of analytical and numerical values of G with increasing load.

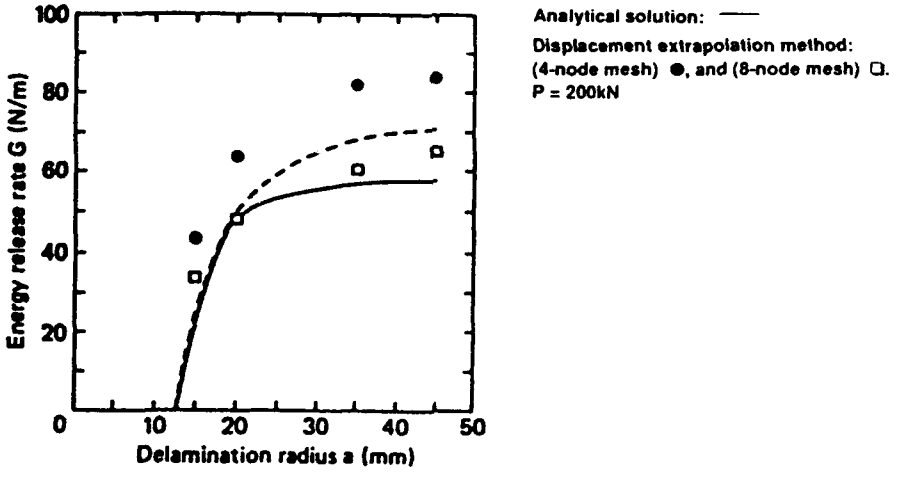

Figure 8. Plot of analytical and numerical values of G with radius.

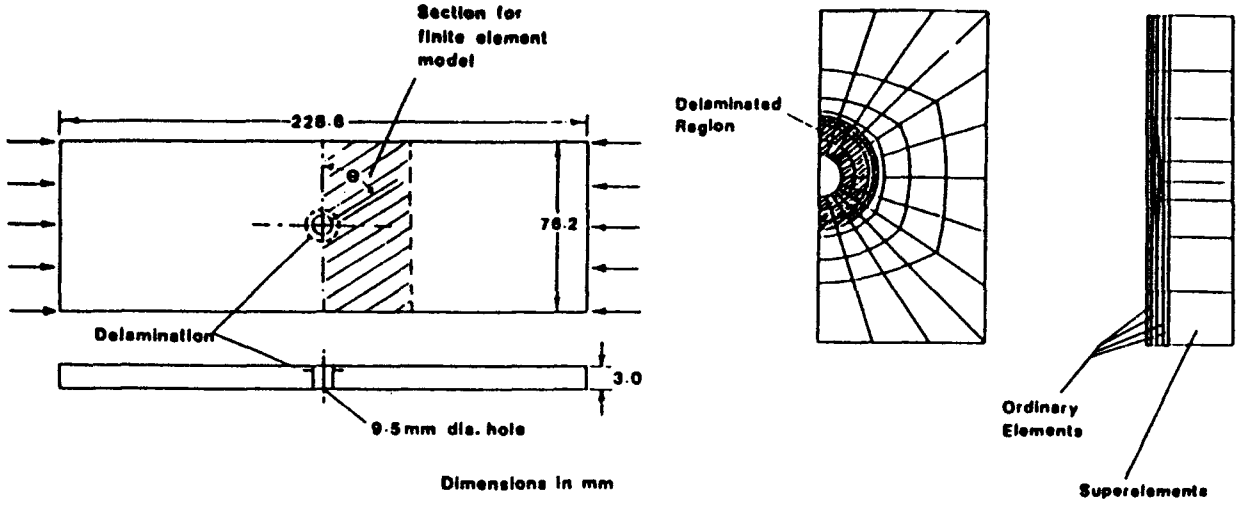

Figure 9. Details of finite element model.

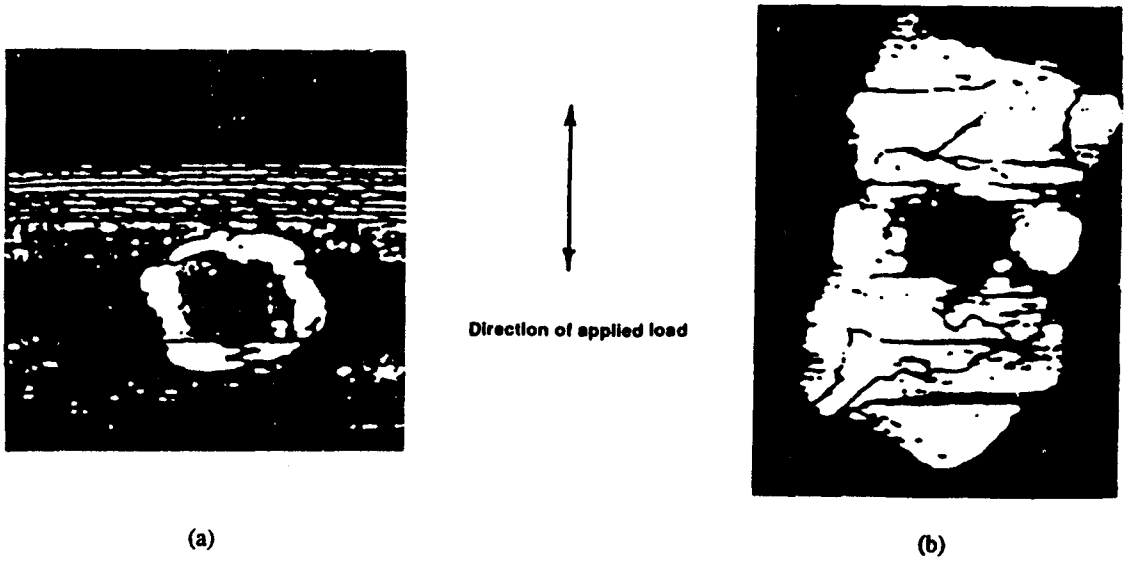

Figure 10. (a) C-scan of initial damage from [15]. (b) C-scan of final delamination growth after 20×10^3 cycles [15].

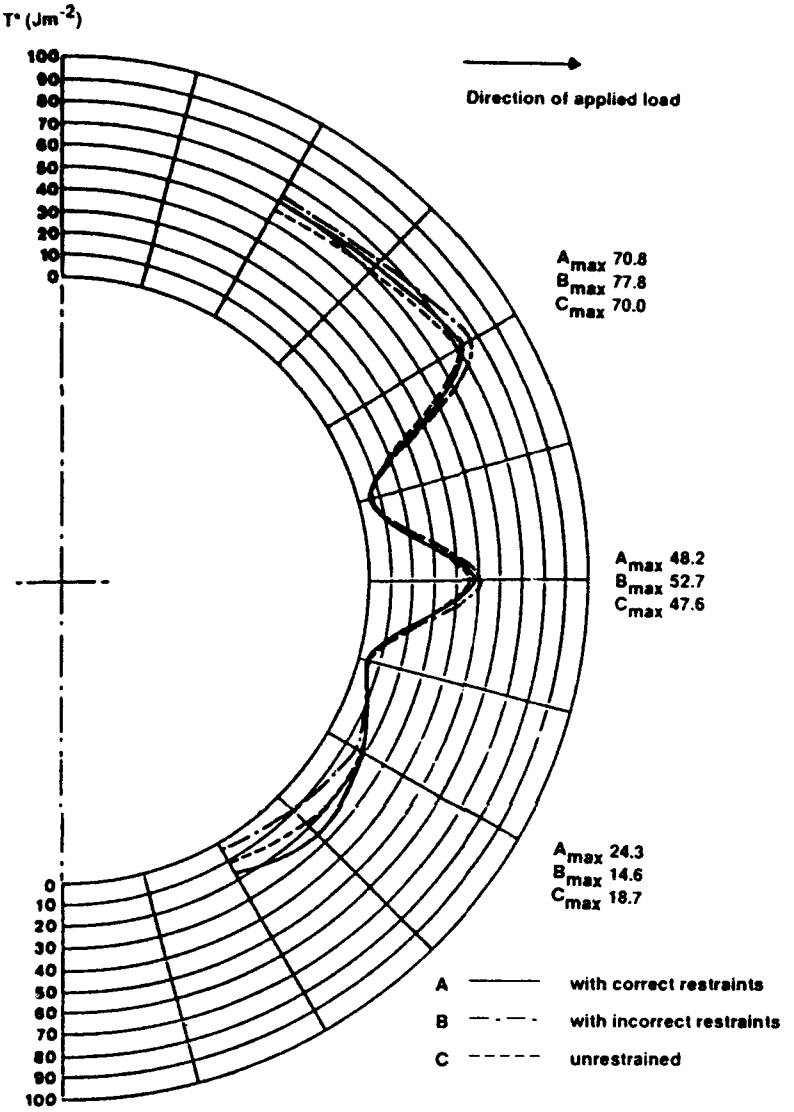

Figure 11. Influence of crack opening restraints on the T^*-integral.

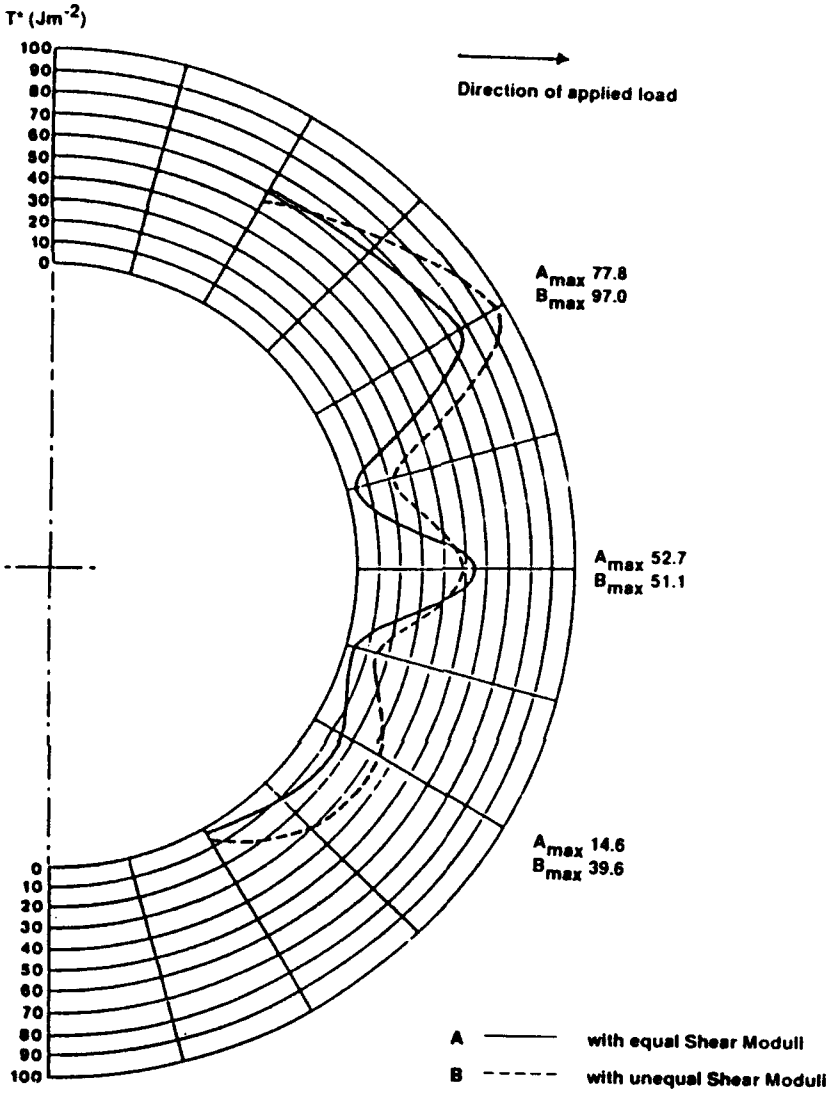

Figure 12. Influence of shear moduli on the T^*-integral.

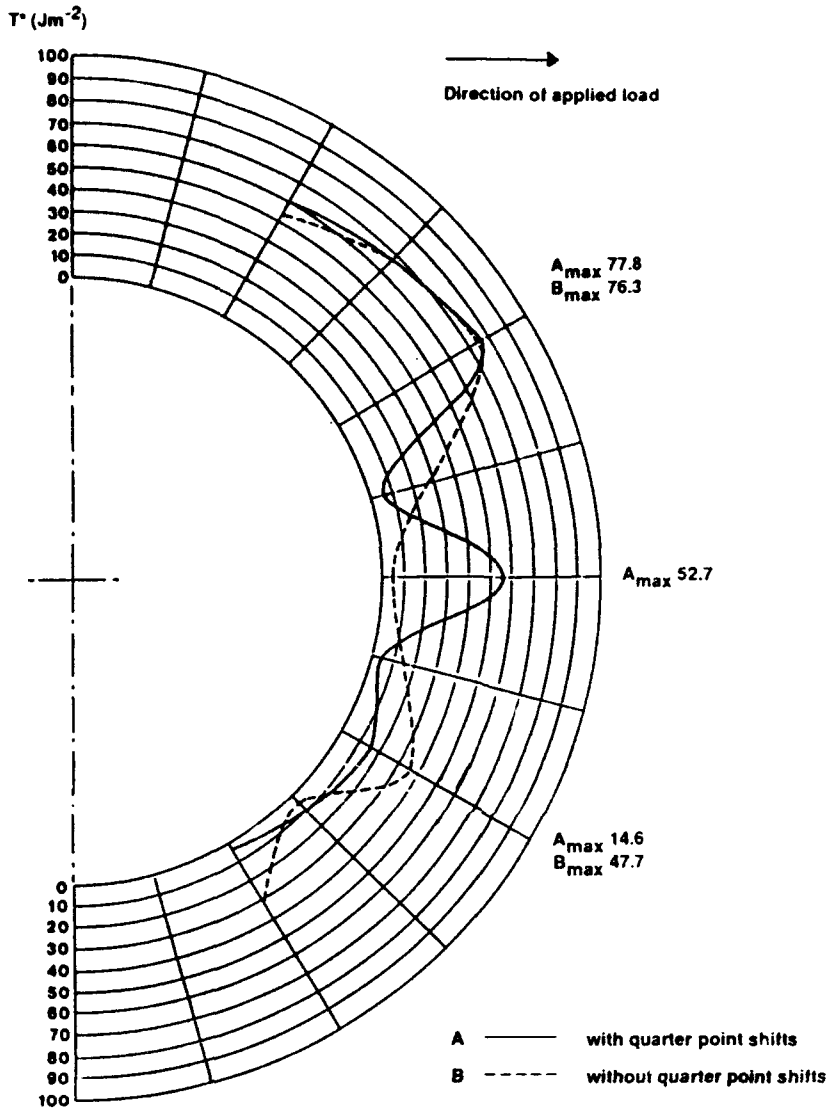

Figure 13. Influence of quarter point shifts on the J^*-integral.

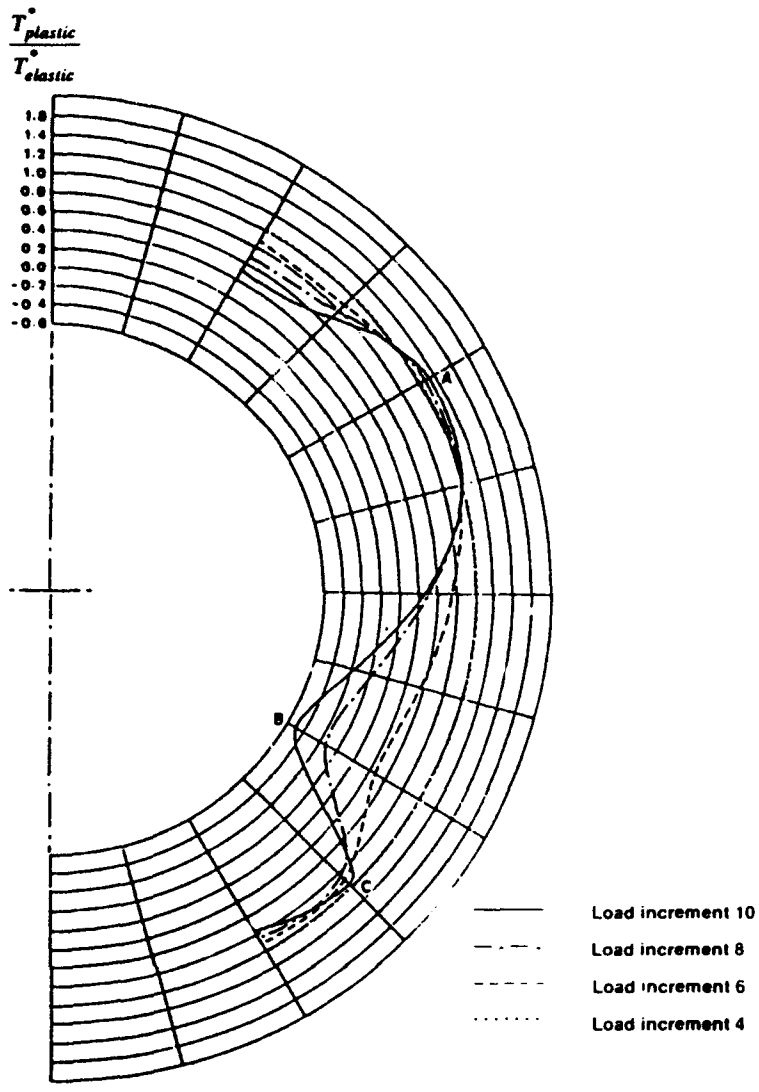

Figure 14. Distribution of $T^*_{plastic}/T^*_{elastic}$ with increasing plasticity.

Figure 15. Damage zone on the CREDP F/A-18 horizontal stabilator.

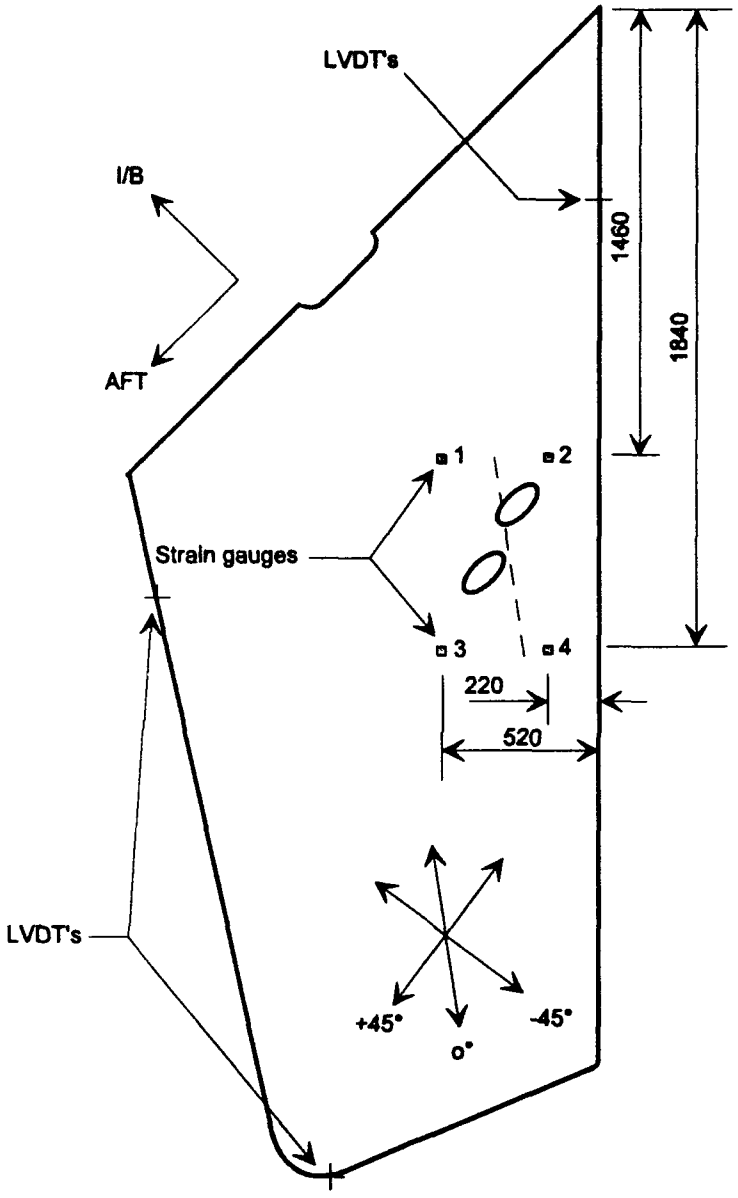

Figure 16. Location of impact damage, strain gauges and displacement transducers on the CREDP F/A-18 horizontal stabilator.

DISTRIBUTION

AUSTRALIA

DEFENCE ORGANISATION

Defence Science and Technology Organisation

Chief Defence Scientist
FAS Science Policy
AS Science Corporate Management
} shared copy

Counsellor Defence Science, London (Doc Data Sheet only)
Counsellor Defence Science, Washington (Doc Data Sheet only)
Senior Defence Scientific Adviser (Doc Data Sheet only)
Scientific Advisor Policy and Command (Doc Data Sheet only)
Navy Scientific Adviser (3 copies Doc Data Sheet only)
Scientific Adviser - Army (Doc Data Sheet only)
Air Force Scientific Adviser
Scientific Adviser to Thailand MRD (Doc Data sheet only)
Scientific Adviser to the DRC (Kuala Lumpur) (Doc Data sheet only)

Aeronautical Research Laboratory
Director
Library
Chief Airframes and Engines Division
Author(s): R. Jones
S. Galea
J. Paul
F. Rose
R. Callinan
R. Chester

Materials Research Laboratory
Director/Library

Main Library - DSTO Salisbury

Defence Central

OIC TRS, Defence Central Library
Document Exchange Centre, DSTIC (8 copies)
Defence Intelligence Organisation
Library, Defence Signals Directorate (Doc Data Sheet Only)

HQ ADF

Director General Force Development (Air)
DDOFFOPS
DSA (Air)
Director Analytical Studies Group

Navy

Director Aircraft Engineering - Navy
Director of Naval Architecture

Air Force

AHQ Air Command (INT1)
PDR AF
DENGPP-AF
AHQ (SMAINTSO)
DGELS AIRREG4 HQLC
OIC CAME HQLC
OIC ATF, ATS, RAAFSTT, WAGGA (2 copies)

UNIVERSITIES AND COLLEGES

Australian Defence Force Academy
Library
Head of Aerospace and Mechanical Engineering

Flinders
Library

LaTrobe
Library

Melbourne
Engineering Library

Monash
Hargrave Library

Newcastle
Library
Head, Institute of Aviation

New England
Library

Sydney
Engineering Library

NSW
Physical Sciences Library

Queensland
Library

Tasmania
Engineering Library

Western Australia
Library

RMIT
Library

University College of the Northern Territory
Library

OTHER GOVERNMENT DEPARTMENTS AND AGENCIES

AGPS
Civil Aviation Authority
Bureau of Air Safety Investigations
Australian Nuclear Science and Technology Organisation
CSIRO: Division of Forest Products

OTHER ORGANISATIONS

NASA (Canberra)
ASTA Engineering, Document Control Office
Ansett Airlines of Australia, Library
Centre for Intelligent Decision Systems
Qantas Airways Limited
Hawker de Havilland Aust Pty Ltd, Victoria, Library
Hawker de Havilland Aust Pty Ltd, Bankstown, Library
Rolls Royce of Australia Pty Ltd, Manager

SPARES (4 COPIES)

TOTAL (70 COPIES)

AL 149 DEPARTMENT OF DEFENCE

DOCUMENT CONTROL DATA

PAGE CLASSIFICATION
UNCLASSIFIED

PRIVACY MARKING

1a. AR NUMBER	1b. ESTABLISHMENT NUMBER	2. DOCUMENT DATE	3. TASK NUMBER
AR-008-409	ARL-TR-23	DECEMBER 1993	AIR 91/056

4. TITLE
ASSESSMENT OF IMPACT DAMAGE IN COMPOSITE STRUCTURES

5. SECURITY CLASSIFICATION (PLACE APPROPRIATE CLASSIFICATION IN BOX(S) IE. SECRET (S), CONF. (C) RESTRICTED (R), LIMITED (L), UNCLASSIFIED (U)).

DOCUMENT	TITLE	ABSTRACT
U	U	U

6. NO. PAGES 54

7. NO. REFS. 77

8. AUTHOR(S)
R.JONES
S.C. GALEA
J.J. PAUL

9. DOWNGRADING/DELIMITING INSTRUCTIONS
Not applicable.

10. CORPORATE AUTHOR AND ADDRESS
AERONAUTICAL RESEARCH LABORATORY
AIRFRAMES AND ENGINES DIVISION
506 LORIMER STREET
FISHERMENS BEND VIC 3207

11. OFFICE/POSITION RESPONSIBLE FOR:
SPONSOR RAAF-DGELS
SECURITY -
DOWNGRADING -
APPROVAL CAED

12. SECONDARY DISTRIBUTION (OF THIS DOCUMENT)
Approved for public release.

OVERSEAS ENQUIRIES OUTSIDE STATED LIMITATIONS SHOULD BE REFERRED THROUGH DSTIC, ADMINISTRATIVE SERVICES BRANCH, DEPARTMENT OF DEFENCE, ANZAC PARK WEST OFFICES, ACT 2601

13a. THIS DOCUMENT MAY BE ANNOUNCED IN CATALOGUES AND AWARENESS SERVICES AVAILABLE TO ....
No limitations.

13b. CITATION FOR OTHER PURPOSES (IE. CASUAL ANNOUNCEMENT) MAY BE [X] UNRESTRICTED OR [ ] AS FOR 13a.

14. DESCRIPTORS

		15. DISCAT SUBJECT CATEGORIES
Composite materials	Impact damage	2011
Laminates	Bonded composite repairs	1104
Damage tolerance	Aeronautical research	

16. ABSTRACT

In order to provide through-life support for structural components fabricated from advanced composite materials, it is desirable to establish a damage tolerance methodology. There are many difficulties in meeting this objective, including the multiplicity of failure modes, the numerous types of potentially significant defects which may arise during manufacture or in service, and the sensitivity to moisture and temp ure. This paper focuses on the problem of impact damage and reviews research undertaken at ARL in recent years related to the analysis and testing of impact damage composite laminates. It is shown that the residual strength of impact damaged laminates reduces to an asymptotic limit as the size of the damage increases and that uniaxial S-N curves for damaged laminates have a generic shape with a pronounced threshold (endurance) level.

PAGE CLASSIFICATION
UNCLASSIFIED
PRIVACY MARKING

THIS PAGE IS TO BE USED TO RECORD INFORMATION WHICH IS REQUIRED BY THE ESTABLISHMENT FOR ITS OWN USE BUT WHICH WILL NOT BE ADDED TO THE DISTN DATA UNLESS SPECIFICALLY REQUESTED.

16. ABSTRACT (CONT).

Recent developments in the bonded repair of impact damage are also discussed and a simple repair methodology is presented. This methodology is then illustrated via a laboratory test program and by a repair to a damaged F/A-18 Horizontal Stabilator.

17. IMPRINT

AERONAUTICAL RESEARCH LABORATORY, MELBOURNE

18. DOCUMENT SERIES AND NUMBER	19. WA NUMBER	20. TYPE OF REPORT AND PERIOD COVERED
Technical Report 23	21 218F	

21. COMPUTER PROGRAMS USED

22. ESTABLISHMENT FILE REF.(S)

23. ADDITIONAL INFORMATION (AS REQUIRED)